

Anti-amyloid activity of amino acid functionalized magnetic nanoparticles on α Lactalbumin aggregation

Andrea Antosova^a, Miroslav Gancar^a, Zuzana Bednarikova^a, Iryna Antal^b, Patrizia Verducci^{c,d}, Olga Parmar^a, Martina Kubovcikova^b, Martina Koneracka^b, Vlasta Zavisova^b, Patrizio Graziosi^c, Barbara Luppi^d, Zuzana Gazova^{a,*}, Eva Bystrenova^{c,*}

^a Department of Biophysics, Institute of Experimental Physics Slovak Academy of Sciences, Watsonova 47, Kosice 040 01, Slovakia

^b Department of Magnetism, Institute of Experimental Physics Slovak Academy of Sciences, Watsonova 47, Kosice 040 01, Slovakia

^c Consiglio Nazionale Delle Ricerche, Istituto Per Lo Studio Dei Materiali Nanostrutturati (CNR-ISMN), via P. Gobetti 101, Bologna 40 129, Italy

^d Department of Pharmacy and Biotechnology, Alma Mater Studiorum, University of Bologna, Via San Donato 19/2, Bologna 40127, Italy

ARTICLE INFO

Keywords:

Amyloid fibril
Magnetic nanoparticle
Amino acid
Atomic force microscopy
Morphology

ABSTRACT

Protein amyloid aggregation involves structural changes in native protein conformers and the formation of amyloid fibrils that accumulate in deposits in the human body. This study explores the effect of magnetic nanoparticles functionalized with amino acids (aaMNPs)—cysteine (Cys), poly-L-lysine (PLL), or proline (Pro)—on the amyloid aggregation of α -lactalbumin (α LA) and its amyloid fibrils (LAF). Our results from thioflavin T fluorescence assay (ThT), atomic force microscopy (AFM), and infrared spectroscopy revealed that the studied aaMNPs inhibit α LA fibrillization and destruct LAF in a concentration-dependent manner. The type of amino acid used for nanoparticle functionalization significantly influences the anti-amyloid efficacy. ProMNPs exhibit the highest inhibitory activity, with the timing of their addition being crucial. Conversely, CysMNPs demonstrate the highest destructing activity. AFM image analysis through grain mapping was employed to quantify the anti-amyloid effects of aaMNPs. Cytotoxicity testing on kidney cells identified PLLMNPs as the only cytotoxic nanoparticles in our study. These findings clarify the mechanisms of inhibition and destruction of LAF in the presence of aaMNPs, which could inform the design of nanoparticles for therapeutic purposes in the future.

1. Introduction

In protein amyloid aggregation, soluble proteins form long, stable fibrils associated with diseases like Alzheimer's and Parkinson's [1,2]. Amyloid fibrils are elongated, unbranched, and highly stable and structured protein fibers consisting of tightly interacting repetitive intermolecular β -sheets arranged into a cross β -structure [3].

The α Lactalbumin (α LA), 123 amino acids long (14.17 kDa) protein belonging to the lysozyme gene protein family, is a predominant protein component of milk and the second most abundant protein in whey [4]. The structure of α LA is stabilized by the presence of four intramolecular disulfide bonds and the binding of calcium [5]. Although not associated with any specific amyloid disease, this protein is well-studied in terms of structure and stability. Kurouski *et al.* already prepared amyloid fibrils using Ca^{2+} -depleted α LA, incubating the protein at pH 2.0 in the presence of 150 mM NaCl at 37°C after 3 days [6].

In recent years, many studies have focused on nanoparticles (NPs) as potential inhibitors of amyloid aggregation [7]. Various synthetic nanoparticles and nanostructures—including gold, graphene, cerium, magnetite, PEGylated NPs, graphene quantum dots, carbon nanotubes, dendrimers, star polymers, polyoxometalates, and nanodiscs—have been explored as inhibitors to combat amyloid aggregation and its associated toxicity in a range of studies, including *in silico*, *in vitro*, *ex vivo*, and *in vivo* [8–13]. Different NPs could variously interfere with the amyloid aggregation of proteins depending on their physico-chemical properties, such as surface area, size, shape, charge, and concentration [14].

Mohammad-Beigi *et al.* emphasized the critical role of electrostatic forces in α -synuclein amyloid fibrillization, noting that charged magnetic NPs (MNPs) can slow or inhibit this process [15]. Superparamagnetic iron oxide NPs (SPIONs) have demonstrated mixed behavior during A β fibrillization. The lower concentrations inhibited

* Corresponding authors.

E-mail addresses: gazova@saske.sk (Z. Gazova), eva.bystrenova@cnr.it (E. Bystrenova).

<https://doi.org/10.1016/j.nanoso.2024.101413>

Received 5 June 2024; Received in revised form 7 November 2024; Accepted 18 November 2024

Available online 29 November 2024

2352-507X/© 2024 The Author(s). Published by Elsevier B.V. This is an open access article under the CC BY license (<http://creativecommons.org/licenses/by/4.0/>).

fibril formation, while higher concentrations led to its acceleration [16]. Cabaleiro-Lago *et al.* showed that the ratio of peptide to NP concentration plays a key role in the dual effects of cationic polystyrene NPs on A β fibrillization [17].

Despite the promising anti-amyloid potential of NPs, their biological safety is not fully elucidated. Factors contributing to NP cytotoxicity include size [18,19], concentration [19], and surface characteristics [20, 21]. Notably, gold NPs and iron oxide NPs have shown lower toxicity compared to other metal oxide nanoparticles. To mitigate cytotoxicity, various molecules - including small proteins, saccharides, amino acids, and organic compounds - are commonly used as coating agents [14].

Amino acids (aa) functionalization of the nanoparticle's surface can improve stability and solubility in aqueous solutions. It enhances their biocompatibility, making them suitable for biomedical applications such as drug delivery, imaging, and therapy [22]. Dubey *et al.* reported that tryptophan- and tyrosine-coated AuNPs inhibited insulin aggregation, whereas free tryptophan and tyrosine amino acids were inactive in inhibiting aggregation [23]. Pradhan *et al.* have shown that glutamine/proline-conjugated MNPs effectively inhibit lysozyme and mutant huntingtin amyloid aggregation [24]. Our previous paper reported that lysine-, glycine-, and tryptophan- MNPs significantly inhibit lysozyme amyloid aggregation and can destroy lysozyme amyloid fibrils [25].

In this work, the amino acids cysteine and proline, and the broadly used biocompatible polymer poly-L-lysine, were used to modify the surface of MNPs. Amino acids were selected based on their specific properties. Cysteine contains sulfhydryl and hydroxyl groups that may interact with hydrophobic regions of proteins. Poly-L-lysine is a synthetic amino acid polymer composed of lysine monomers with a basic side chain. Proline contains a five-membered ring and is known as a breaker of β -sheet protein structure, which forms the core of amyloid fibrils.

We have examined the physico-chemical properties [26] (hydrodynamic diameter, zeta potential, and isoelectric point) of prepared amino acid-functionalized magnetic nanoparticles (aaMNPs) to evaluate the impact of different amino acid functionalization on their properties. The ability of aaMNPs to inhibit α Lactalbumin amyloid fibrillization (inhibitory effect) and destruction of α Lactalbumin amyloid fibrils (LAF) (depolymerizing effect) were monitored using thioflavin T (ThT) fluorescence assay and atomic force microscopy (AFM) techniques. LAFs were prepared in 100 mM CaCl₂ at pH 2.0. The preparation conditions were chosen based on our previous work [27]. Globular proteins such as α LA are very stable under physiological conditions; therefore, we need more aggressive conditions to prepare amyloid fibrils, such as acidic pH, elevated temperature, and mixing. The kinetics of α LA fibrillization alone and in the presence of aaMNPs were assessed using ThT to shed light on their inhibitory mechanism. Attenuated total Reflection Fourier-transform infrared spectroscopy (ATR-FTIR) spectroscopy in the amide I region was used to study the protein secondary structure of α LA aggregates after the treatment of aaMNPs. Moreover, the effect of studied aaMNPs on HEK293 kidney cell viability was determined. For the first time, an effect of NPs is investigated in the process of α LA amyloid fibrillization, and statistical AFM analysis is performed.

2. Results and discussion

2.1. Characterization of amino acids functionalized magnetic nanoparticles (aaMNPs)

The iron oxide MNPs stabilized with perchloric acid were synthesized using a standard coprecipitation method [28]. The aaMNPs: cysteine (Cys), proline (Pro), and poly/amino acid poly-L-lysine (PLL) were prepared by mixing MNPs with a solution of a given amino or poly/amino acids at room temperature. The procedure is described in detail in our previous studies [29].

Atomic force microscopy (AFM) was used to visualize the

morphology and determine the size distribution of aaMNPs. Uncoated MNPs were characterized in our previous work with a diameter of 7.6 ± 0.39 nm. Typical AFM images of aaMNPs are shown in Fig. 1a in a grey inverted scale. The images display individual nanoparticles, clusters, or larger agglomerates; these higher complexes are the most evident for ProMNPs. Histograms of diameter distribution with Gaussian fit from a set of relative AFM images are shown in Fig. 1b. Diameters were calculated from the minimum circumcircle radius of grains (the radius of a minimum circle that contains the grain). The diameters of 60 nm (CysMNPs), 37 nm (PLLMNPs), and 45 nm (ProMNPs) result from the maximum value of the Gaussian function. The broad peak of ProMNPs confirms their tendency to aggregate on mica.

The dynamic light scattering (DLS) technique was employed to obtain their hydrodynamic diameter (D_H). The hydrodynamic diameters of the aaMNPs presented in Table S1a, are equal to 70.0 nm (CysMNPs), 50.4 nm (PLLMNPs), and 42.0 nm (ProMNPs) compared to uncoated MNPs that have 28.4 nm. The differences in the diameters measured by the two experimental techniques are related to the fact that DLS provides the average hydrodynamic diameter, including the solvation layer around the nanoparticles. In contrast, AFM provides the physical diameter of the nanoparticles.

The laser Doppler velocimetry was used to measure zeta potential (ζ) values and isoelectric point (pI) to monitor amino acid adsorption on MNPs and the stability of samples. The obtained data determined in the buffer used for α LA amyloid fibril preparation (100 mM CaCl₂, pH 2.0) are shown in Table S1a. The high positive zeta potential values observed for all studied aaMNPs (20.7 mV for CysMNPs, 46.0 mV for PLLMNPs, and 32.9 mV for ProMNPs) indicate the high stability of aaMNPs in this buffer. The acidic pH enhances stability due to the presence of a sufficient positive charge. The ζ value $> +30$ mV ensures that nanoparticles remain apart from each other, eliminating the possibility of agglomeration, aggregation, and/or flocculation [30]. Zeta potential measurement as a function of pH was performed to confirm the surface charge properties and the presence of amino groups on the surface of the MNPs. These ζ vs. pH dependencies were used to determine the pI of aaMNPs (pH at which a nanoparticle carries no net electrical charge) CysMNPs = 5.1, PLLMNPs = 9.7 and ProMNPs = 6.6. The shift of pI compared to bare MNPs (pI_{MNPs} = 6.9) in Table S1a also confirms the adsorption of amino acids on the surface of MNPs.

In our study, we have evaluated how the presence of aaMNPs influences the α LA amyloid fibrillization process (inhibitory activity) and how nanoparticles interfere with mature LAF (depolymerization activity). The experimental conditions for these studies are different (see Experimental section).

AFM images (Figure S1) show the morphology of aaMNPs under various conditions. In inhibitory assays (at pH 2.0, 65°C), a slight increase in deposited PLLMNPs is seen after 25 minutes, along with reduced ProMNPs clustering. After 180 minutes, clustering increases for all aaMNPs. For depolymerization assays (at pH 2.0, 37°C), a slight increase in deposited aaMNPs is visible, with ProMNPs showing observable on mica.

ATR-FTIR analysis confirmed amino acid binding on MNPs' surface (Fig. 1c). Characteristic peaks included NH₂ stretching at 3300 cm⁻¹ and carboxylate asymmetric ($\nu_{as}(\text{COO}^-)$) and symmetric ($\nu_s(\text{COO}^-)$) stretching at 1600 cm⁻¹ and 1400 cm⁻¹, respectively. MNPs' presence was indicated by a strong absorption band at 550–600 cm⁻¹ for Fe-O bond vibration. The role of the carboxyl group in binding was evident in the wavenumber difference ($\Delta \nu$) between asymmetric and symmetric carboxyl stretches, varying with coordination. Spectral shifts in CysMNPs, PLLMNPs, and ProMNPs confirmed functionalization. Wavenumber separations (Δ) of 227 cm⁻¹ for CysMNPs and 208 cm⁻¹ for ProMNPs suggested a monodentate COO⁻ interaction with MNPs' surface. MNPs' Fe-O bond stretching modes at approximately 538 cm⁻¹ (CysMNPs), 540 cm⁻¹ (PLLMNPs), and 544 cm⁻¹ (ProMNPs) validated successful amino acid coating. Our data showed that the surface functionalization of MNPs with selected amino acids leads to variability in

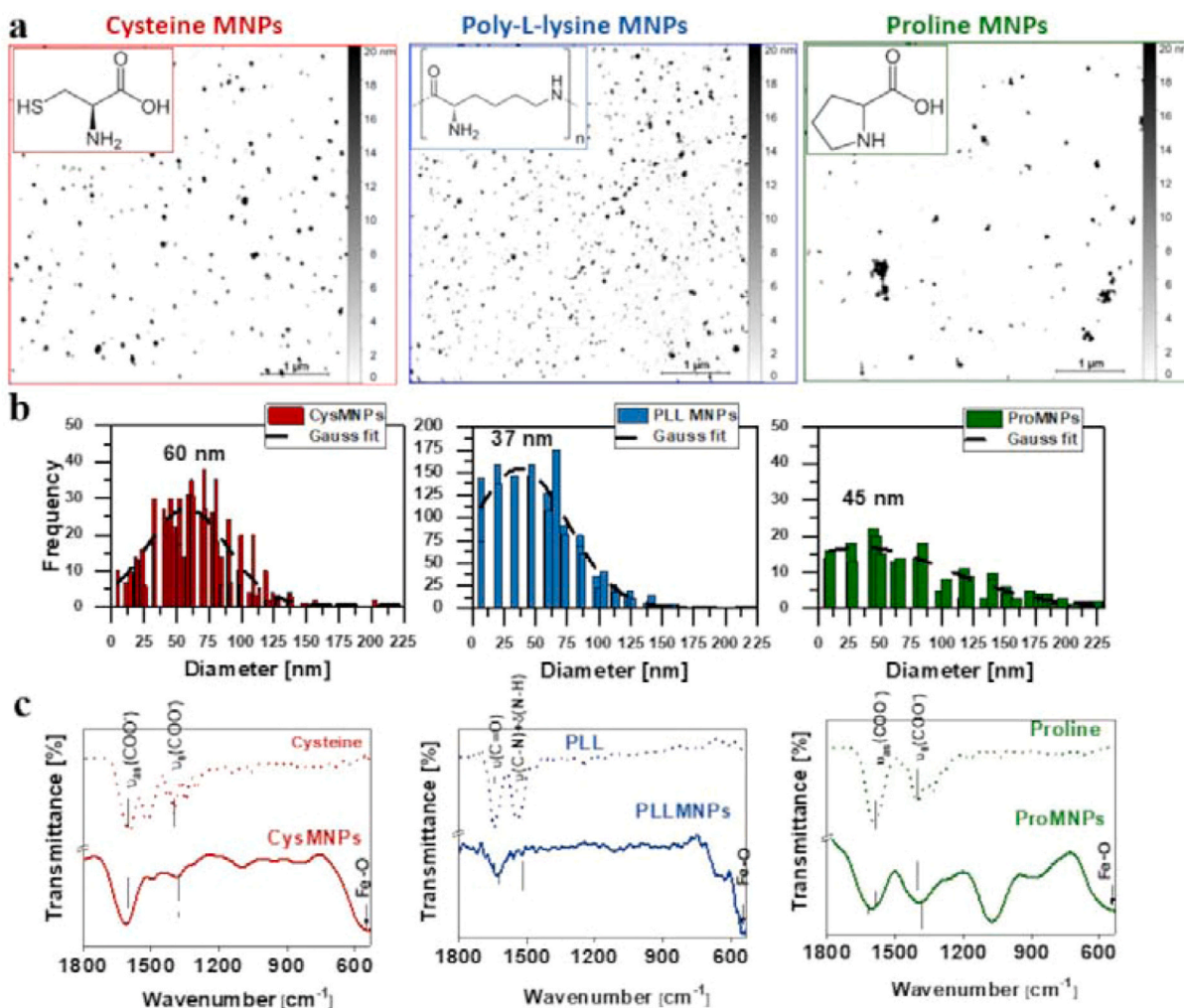


Fig. 1. a) Typical AFM images of magnetic nanoparticles functionalized by: CysMNPs (red), PLLMNPs (blue), ProMNPs (green). All images are 5×5 μm with a scale bar representing 1 μm. The concentration of aaMNPs was 7 μg.mL⁻¹. b) Histogram of diameter distribution with Gaussian fit from relative AFM images. c) The FTIR spectra of free amino acid (dotted line) and aaMNPs (solid line): cysteine and CysMNPs (red), PLL and PLLMNPs (blue), and proline and ProMNPs (green).

the size, zeta potential, and charge of the prepared aaMNPs. Changes in pI and shift of absorption bands in the FTIR spectra confirmed the binding of amino acids to the magnetite core.

The potential toxicity of newly developed aaMNPs is a key factor that limits their use in nanomedicine [31]. Nanoparticle toxicity depends on factors like size, charge, and targeting [32–34]. Uncoated MNPs showed no toxicity on HEK293 cells [35]. We assessed the cytotoxicity of aaMNPs on HEK293 cells, Figure S2. CysMNPs and ProMNPs showed minimal toxicity, PLLMNPs were the most toxic, with 21.8 % cell viability at 50 μg.mL⁻¹ concentration of these MNPs. The lethal dosage LD₅₀ for PLLMNPs is >25 μg.mL⁻¹, consistent with results from similar experiments on various cancer cell lines [36]. PLL is commonly used for cell culture applications due to its ability to enhance cell adhesion and proliferation. However, its high positive charge density may also lead to interactions with cellular components that induce cytotoxic effects [37]. In contrast, cysteine and proline may exhibit lower cytotoxicity due to their roles as naturally occurring amino acids in biological systems. Cysteine has been used in several studies as a coating agent for various metal- and polymer-based NPs, showing minimal cytotoxicity. For example, Liu *et al.* designed a cysteine-coated CdSe(ZnCdS) quantum dots, where cysteine coating enabled the NPs to be biologically compatible, easily functionalized, and cleared via renal pathways, minimizing toxicity in rat models [38]. Magnetite nanoparticles coated with L-cysteine were used as a support matrix for the immobilization of

Candida antarctica Lipase A [39]. On the other hand, to our knowledge, proline is usually used as a coating agent for particles designed for various catalytic applications [40]. Proline-coated gold NPs were used as a highly efficient nanocatalyst for the enantioselective direct aldol reaction in water [41].

2.2. Anti-amyloid activity of uncoated MNPs and aaMNPs on αLactalbumin amyloid fibrils

2.2.1. Inhibition of αLA amyloid aggregation by MNPs and aaMNPs

ThT fluorescence assay was used to investigate the inhibitory effect of aaMNPs compared to uncoated MNPs against αLA amyloid aggregation (Fig. 2a). The concentration of αLA in the inhibition assay was kept at a constant value of 20 μM (284 μg.mL⁻¹). The αLA to MNPs/aaMNPs concentration (taken to magnetite) ratios range from 2 to 4260 μg.mL⁻¹. Presented data indicate that uncoated MNPs and aaMNPs dose-dependently inhibited αLA amyloid fibrillization as relative ThT fluorescence values are decreasing with increasing concentration of MNPs/aaMNPs. Similar dose-dependent inhibitory activity was observed for AuNPs [42], curcumin-functionalized gold [43] and magnetic NPs coated with dextran [44], trisodium acetate [45], and glycine [46] on β-lactoglobulin and HEWL amyloid aggregation. The MNPs/aaMNPs' inhibitory efficiency was quantified by IC₅₀ values (a concentration of MNPs/aaMNPs leading to a 50 % decline in ThT fluorescence intensities,

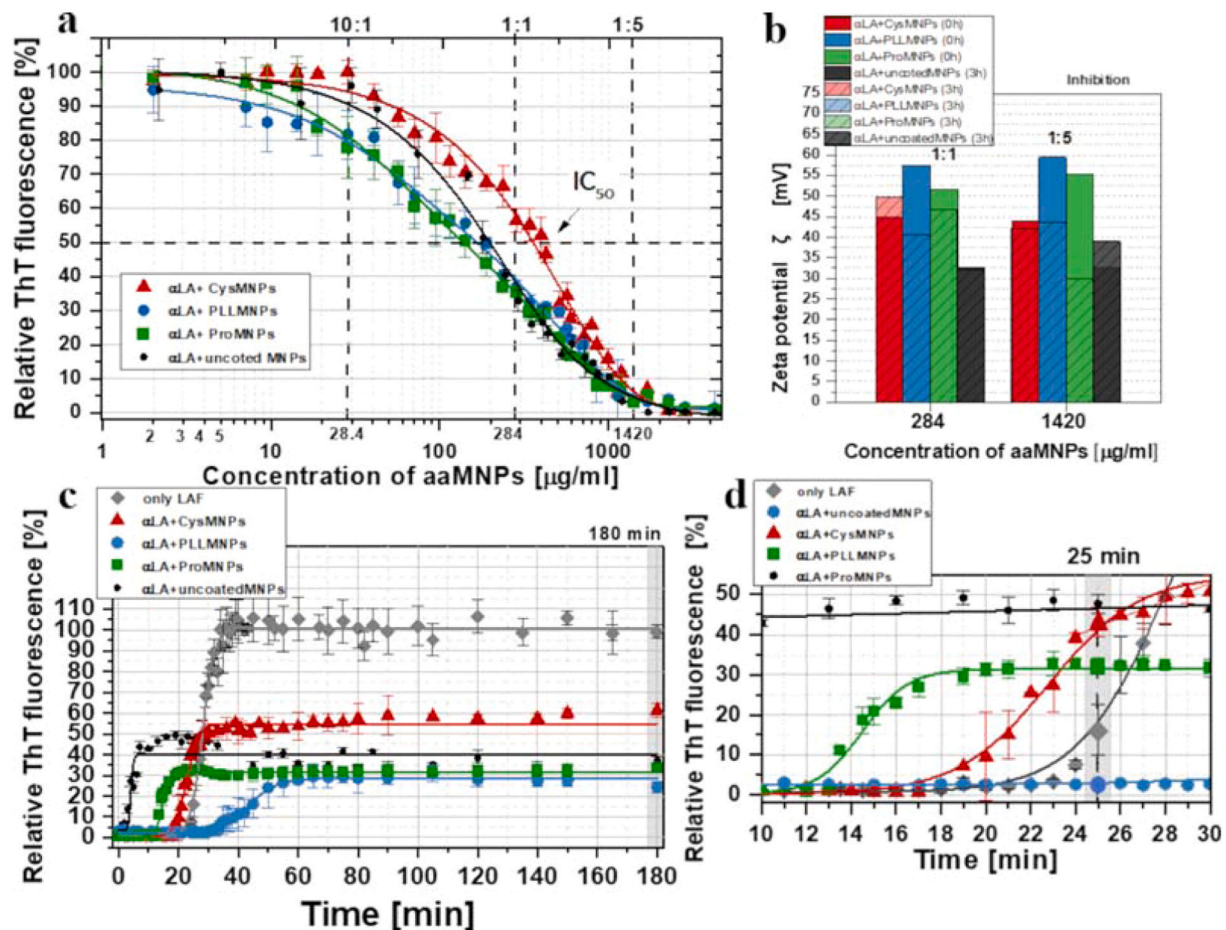


Fig. 2. a) Relative ThT fluorescence detected for α LA amyloid fibrillization in the presence of an increasing concentration of CysMNPs (red triangles), PLLMNPs (blue circles), ProMNPs (green squares) and uncoded MNPs (black circles). The concentration of α LA was 20 μ M (284 μ g.mL⁻¹). The average values of fluorescence intensities ($n = 6$) were normalized to the untreated α LA (taken as 100 %). b) Zeta potential of uncoded MNPs and aaMNPs alone and in mixtures with α LA; at two α LA:aaMNPs ratios 1:1 and 1:5; after 0 h (full colour bars) and after 180 min (dashed colour bars) incubation at 65°C and 1200 rpm. c) Kinetic profiles of α LA amyloid fibrillization alone (grey diamonds) and in the presence of CysMNPs (red triangles), PLLMNPs (blue circles), ProMNPs (green squares) and uncoded MNPs (black circles) (w/w ratio α LA:aaMNPs = 1:1). The error bars represent the average deviation of multiple measurements ($n = 6$). d) Detailed view of the first 30 min of kinetics.

indicating the formation of 50 % fibrils).

The most significant inhibition of α LA amyloid fibrils formation was observed for the smallest ProMNPs ($IC_{50} = 134.6 \pm 5.6 \mu$ g.mL⁻¹), followed by PLLMNPs ($IC_{50} = 159.9 \pm 7.3 \mu$ g.mL⁻¹). The weakest effect has been shown for the CysMNPs ($IC_{50} = 332.2 \pm 8.9 \mu$ g.mL⁻¹). Compared with uncoded MNPs ($IC_{50} = 191.3 \pm 4.8 \mu$ g.mL⁻¹), the functionalization of MNPs by proline and polylysine improved the inhibitory activity of NPs. However, functionalization by cysteine reduced the inhibitory activity of MNPs, likely due to interactions between the protein cysteine residues and those on the CysMNPs, potentially forming disulfide bonds. Obtained IC_{50} values are summarized in Table 1. It is worth noting that the amino acids alone (not bound to MNPs surface) do not possess inhibitory activity towards α LA fibrillization even at the highest

concentration (data not shown). Our data suggest that the combination of NP size, stability and dispersity, and interactions between α LA and aaMNPs are essential for effectively inhibiting α LA amyloid fibrillization. The importance of NP size in inhibiting amyloid aggregate formation has also been highlighted in other studies. For example, Gao *et al.* demonstrated that while large gold NPs (36 nm) accelerated A β aggregation, smaller NPs (6 nm) significantly delayed or even inhibited the aggregation process [47]. On the contrary, Kim *et al.* observed that very large NPs (80 nm) produced large amorphous peptide aggregates, while smaller NPs (20 nm) led to protofibril formation [48].

To better explain the inhibitory activity of uncoded MNPs and aaMNPs, the kinetics of α LA amyloid fibrillization was monitored by ThT emission intensity over the course of 3 h incubation of native α LA

Table 1

IC_{50} values and kinetic parameters derived from aggregation kinetics of α LA in the presence of aaMNPs. Every experiment was performed six times, and the final data represented an average value accompanied by a corresponding deviation. t_{LAG} represents a lag time of aggregation, t_{HALF} stands for aggregation half-time, and k_{AGG} is the aggregation rate constant.

INHIBITION	α LA	α LA+uncodedMNPs	α LA+CysMNPs	α LA+PLLMNPs	α LA+ProMNPs
IC_{50} [μ g.mL ⁻¹]		191.3 \pm 4.8	332.2 \pm 8.9	159.9 \pm 7.3	134.6 \pm 5.6
t_{LAG} [min]	24 \pm 0.2	1.13 \pm 0.7	18.7 \pm 0.3	34.0 \pm 0.7	12.5 \pm 0.2
t_{HALF} [min]	28 \pm 0.1	3.7 \pm 0.4	22.7 \pm 0.1	43.4 \pm 0.4	14.5 \pm 0.1
k_{AGG} [min ⁻¹]	0.5 \pm 0.03	0.8 \pm 0.20	0.5 \pm 0.04	0.2 \pm 0.02	1.0 \pm 0.11

alone or in the presence of MNPs/aaMNP at concentration ratio 1:1 (α LA:MNP/aaMNP).

As shown in Fig. 2c (grey curves), the α LA amyloid formation follows characteristic nucleation-polymerization model, with three distinct phases: initial nucleation characterized by lag time (t_{LAG}), elongation phase described by aggregation half-time (t_{HALF}), and aggregation constant (k_{AGG}) parameters. In the third phase, the plateau, fluorescence values reach equilibrium, indicating the presence of mature amyloid fibrils. The kinetic parameters of α LA amyloid fibrillization alone and in the presence of uncoated MNPs and aaMNP are summarized in Table 1. For α LA, the 24-minute long lag phase is followed by a rapid elongation phase characterized by $t_{HALF} = 28 \pm 0.1$ min and aggregation constant $k_{AGG} = 0.5 \pm 0.3 \text{ min}^{-1}$.

Adding MNPs/aaMNP at the beginning of the aggregation process ($t = 0$ min) led to significant kinetics changes. In Fig. 2c (in the detailed view in Fig. 2d), the presence of uncoated MNPs (black squares), CysMNP (red triangles), and ProMNP (green squares) presumably catalyze the nucleation processes of α LA as evidenced by shorter lag phases (Table 1) compared to the untreated α LA. On the contrary, PLLMNP (Fig. 2c, blue circles) prolong the lag phase $t_{LAG} = 34 \pm 0.7$ min, thus delaying the overall formation of amyloid aggregates. The t_{HALF} parameters analogically followed the trend of t_{LAG} : MNPs < ProMNP < CysMNP < PLLMNP. The aggregation constants determined for MNPs and ProMNP were higher compared to untreated α LA. Contrarily, the PLLMNP's k_{AGG} was lower, and CysMNP's k_{AGG} was comparable to untreated α LA (Table 1). All aaMNP and uncoated MNPs caused a significant decrease in steady-state fluorescence values in correlation with ThT intensities obtained from concentration dependencies.

To elucidate which step of the α LA aggregation pathway is affected, we have monitored the kinetics of α LA fibrillization after adding MNPs/aaMNP in different stages of amyloid aggregation. The goal was to

identify the ability of MNPs/aaMNP to interact with different α LA pre-fibrillar species and, thus, influence the fibrillization progression. Therefore, the uncoated MNPs and aaMNP were added to the aggregation mixture at two time points during the α LA lag phase ($t = 10$ and 15 min; triangles and stars) in addition to $t = 0$ min (Fig. 3). The time points were selected based on the kinetics profile of α LA alone (Fig. 2c, grey curve). As mentioned earlier, adding uncoated MNPs, CysMNP, and ProMNP at the beginning of the process shortened the lag phase, indicating catalysis of the pre-fibrillar species formation (Fig. 3).

The addition of CysMNP (shades of red) and ProMNP (shades of green) later during the lag phase (t_0 – squares, t_{10} – triangles, and t_{15} – stars) resulted in its prolongation (by ~ 7 and 12 min, respectively), roughly matching the untreated α -LA upon addition at $t = 15$ min (Fig. 3b, d). We also observed such behavior in the case of uncoated MNPs (shades of black) (Fig. 3a). Still, even though their addition at $t = 15$ min resulted in the most pronounced, ~ 14 minutes, lag phase elongation, they simply induced the amyloid aggregation at the point of their addition. These results indicate that adding uncoated MNPs, CysMNP, and ProMNP closer to the end of the lag phase can suppress their unwanted catalytic activity. The addition of PLLMNP after 10 minutes had no significant impact on lag phase duration (blue triangles in Fig. 3c) while increasing the aggregation rate compared to the addition at $t = 0$ min. Moreover, the steady-state ThT intensity values are significantly higher, suggesting a higher amount of formed aggregates. Furthermore, introducing PLLMNP at $t = 15$ min resulted in an instantaneous, rapid elongation phase and effectively shortened the lag phase even compared to the untreated α LA (cyan stars in Fig. 3c). Unlike in the case of PLLMNP, the fluorescence upon adding uncoated MNPs, CysMNP, and ProMNP at different time points are comparable to fluorescence values observed after introduction at $t = 0$ min, suggesting that the addition time does not affect the aggregation results. From kinetic experiments, we conclude that uncoated MNPs and aaMNP

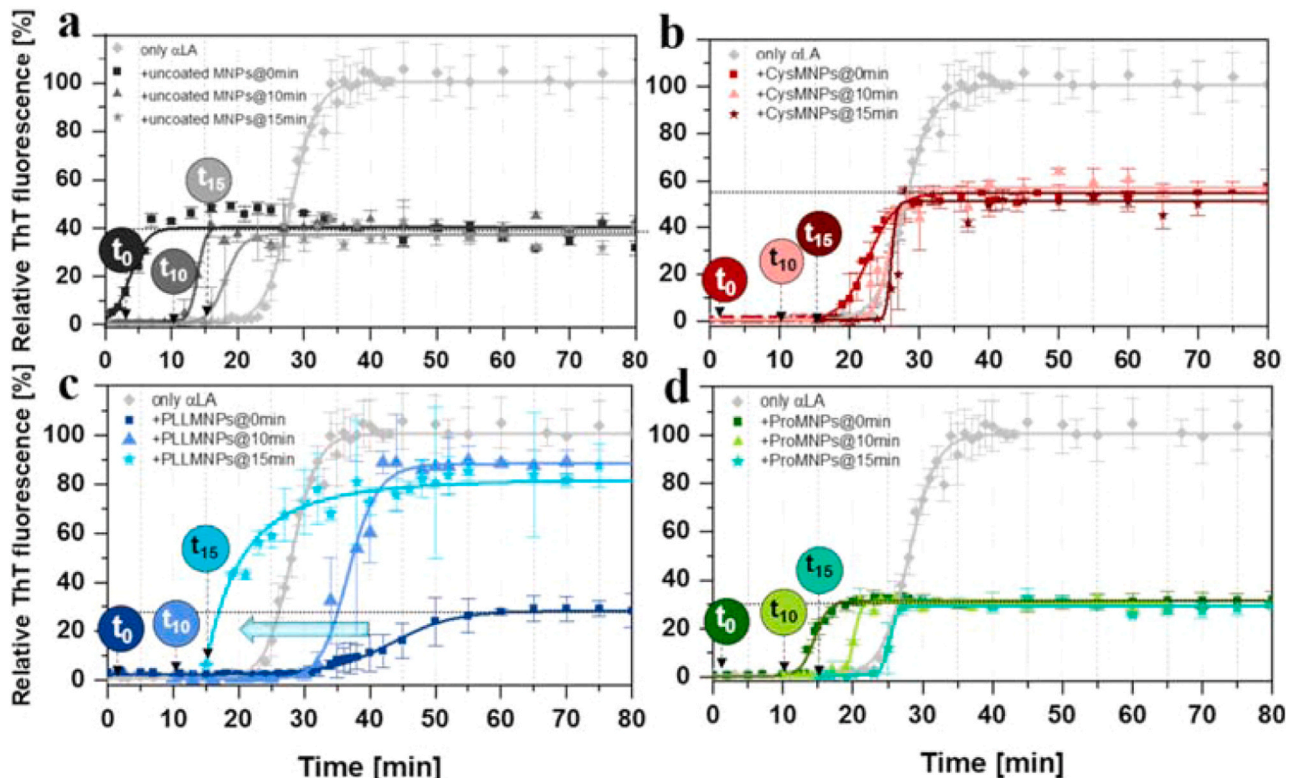


Fig. 3. Kinetic profiles of α Lactalbumin amyloid fibrillization alone (grey squares in each figure) and in the presence of **a)** uncoated MNPs, **b)** CysMNP, **c)** PLLMNP, and **d)** ProMNP (ratio w/w α LA: aaMNP = 1:1) added in different times ($t = 0, 10$ and 15 min) of α LA fibrillization. Data were obtained using ThT assay. The error bars represent the arithmetic deviation for repeated measurements of six separate samples. The curves were obtained by fitting the average experimental values using 4-parameter logistic equation in OriginPro software.

interact with pre-fibrillar and fibrillar species in a different manner. When added at $t = 0$, MNPs/aaMNPs interact primarily with monomeric α LA. In this case, PLLMNPs were the most effective, significantly prolonging the lag phase, while uncoated MNPs, CysMNPs, and ProMNPs displayed amyloid-inducing behavior. Adding uncoated MNPs at later time points resulted in a lag phase shift to longer times; however, lag times only correlate to the addition times. The delayed addition of CysMNPs and ProMNPs (after 15 min incubation) apparently suppressed their amyloid-inducing properties, effectively elongating the lag phase. The most striking difference was observed in the case of PLLMNPs, losing their inhibition efficacy at later addition times, suggesting that they almost exclusively bind monomeric α LA. Overall, the functionalization of bare MNPs enhanced their anti-amyloid efficacy (with the exception of CysMNPs). Assessment of their addition time reduced their amyloid-inducing effect (lag phase shortening). Moreover, in the case of ProMNPs (all time points) and PLLMNPs (t_0), we observed a ~ 10 – 12 % reduction in the number of fibrils formed compared to uncoated MNPs, in agreement with their lower IC_{50} values. (Fig. 3a, c, d). Obtained results are in good agreement with published data for positively charged MNPs, which promoted the fibrillization of A β peptide [16].

All studied aaMNPs displayed concentration-dependent inhibition effects. CysMNPs exhibited the weakest inhibitory activity, likely binding weakly with monomers. Moreover, the aggregation pathway was only slightly influenced (t_{LAG} and t_{HALF} comparable to α LA). Similar results were observed for cysteine-modified carbon NPs [49]. PLLMNPs bound α LA more effectively, leading to a lower number of free monomers in bulk available for aggregation prolonging the lag phase and causing a significant reduction of fibril load (the longest t_{LAG} and second lowest IC_{50} values). ProMNPs also significantly shortened lag phases and reduced amyloid fibril formation, presumably by binding monomers or pre-fibrillar species. We assume that this adsorption might lead to two simultaneously acting effects: decreasing the number of free monomers (the lowest IC_{50} values) and providing an environment for the monomers to form short-lifetime oligomers, accelerating the formation of amyloid fibrils (the shortest t_{LAG} and the steepest elongation phase

indicated by the highest k_{AGG}). Published studies support the inhibitory potential of our aaMNPs, as proline-coated NPs demonstrated to inhibit amyloid fibril formation by blocking oligomer formation and binding to amyloidogenic regions through various interactions [24,50]. Similarly, NPs coated with amino acids containing cyclic structures have shown significant inhibitory activity [23].

Various types of metal and carbon NPs, can modify the nucleation phase of amyloid fibril formation by providing an additional surface or by interacting with amyloid peptides, thus promoting the aggregation. For instance, some studies found that carbon-based NPs could reduce the lag phase in the A β aggregation, suggesting a similar mechanism [51]. Additionally, NPs' size and surface characteristics can affect the aggregation dynamics of proteins. Smaller NPs tend to be more effective in delaying fibril formation compared to larger ones, as they provide a larger surface area for interaction [14,52]. These findings support our results as PLLMNPs exhibited the longest lag phase when added at the beginning of the aggregation or in early stages of the lag phase (Fig. 3c, t_0 and t_{10}). Moreover, the catalytic role of NPs in protein aggregation has been discussed in the context of enhancing nucleation by stabilizing intermediates or promoting conformational changes in the protein [14, 53,54].

2.2.2. Destruction of α Lactalbumin amyloid fibrils by MNPs and aaMNPs

In addition to inhibiting the formation of amyloid aggregates, we were also interested in the destructive activity of uncoated MNPs and aaMNPs on mature amyloid fibrils. The formed LAF (10 μ M) were treated with aaMNPs in a broad concentration range for 24 h. The ability of MNPs/aaMNPs to interfere with mature LAF was assessed using the thioflavin T (ThT) fluorescence assay to determine DC_{50} values (a concentration of MNPs/aaMNPs that leads to a 50 % decrease in fluorescence intensity corresponding to the destruction of 50 % fibrils). Fig. 4a plots the relative ThT fluorescence of LAF+MNPs/aaMNPs complexes: CysMNPs (red triangles), PLLMNPs (blue circles), ProMNPs (green squares) and uncoated MNPs (black squares) against MNPs/aaMNPs concentration. As the concentration of MNPs/aaMNPs increases,

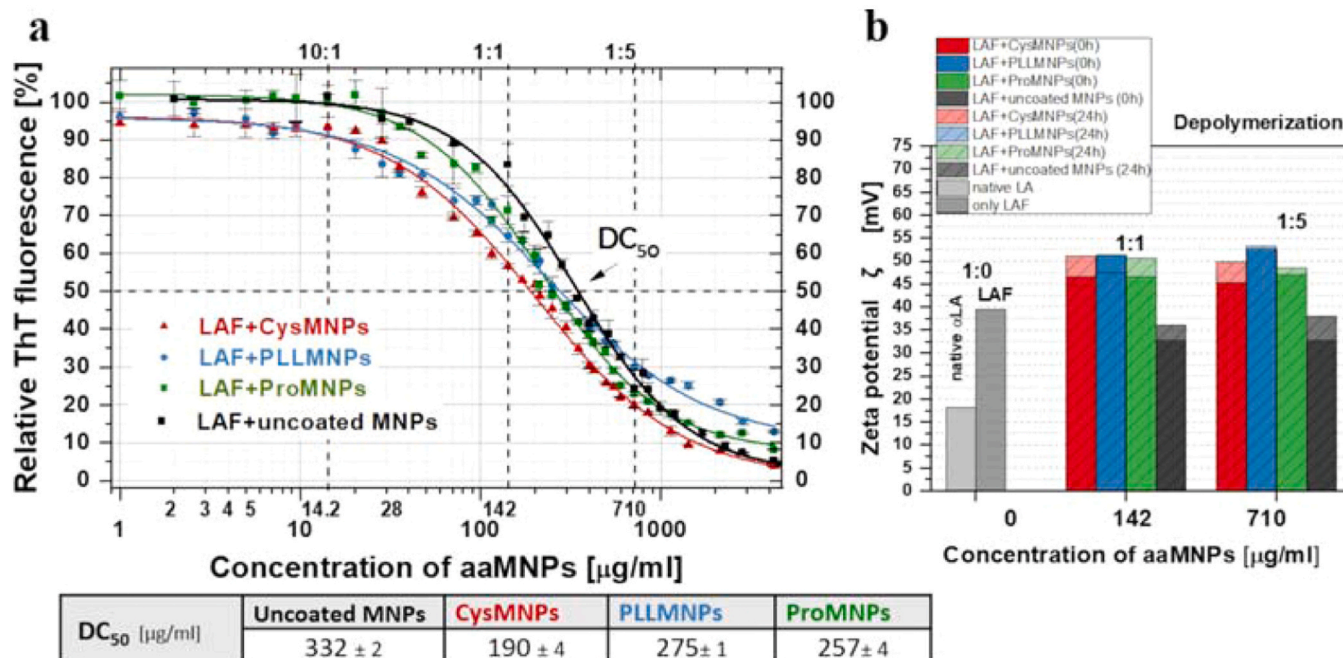


Fig. 4. a) Relative ThT fluorescence detected for LAF in the presence of an increasing concentration of CysMNPs (red triangles), PLLMNPs (blue circles), and ProMNPs (green squares) after 24 h at 37° C. The concentration of LAF was constant 10 μ M (142 μ g. ml^{-1}). The average values of fluorescence intensities obtained from six independent measurements were normalized to the untreated LAF (taken as 100 %). The curves were obtained by fitting the average values using a non-linear least-squares method. In the table, values DC_{50} are reported. b) Zeta potential measured for MNPs/aaMNPs alone and in mixtures with LAF after 24 h at 37° C for different concentrations ratios of LAF to nanoparticles.

relative ThT fluorescence decreases, suggesting a concentration-dependent destroying effect. Obtained DC_{50} values are listed in Fig. 4. The strongest destroying effect with the lowest DC_{50} ($DC_{50} = 190 \pm 4 \mu\text{g.mL}^{-1}$) was observed for CysMNPs. The higher DC_{50} values, except uncoated MNPs, were determined for PLLMNPs ($DC_{50}=275 \pm 1 \mu\text{g.mL}^{-1}$) and ProMNPs ($DC_{50}=257 \pm 4 \mu\text{g.mL}^{-1}$). The highest DC_{50} was observed for uncoated MNPs ($DC_{50} = 332 \pm 2 \mu\text{g.mL}^{-1}$), which implies that the functionalization of MNPs with the studied amino acids improved the destructive activity of MNPs on LAF.

Concentration ratios of LAF:aaMNPs = 10:1 (where no or minimal destructive effects on the DC_{50} curve are observed), 1:1 (where a 30–45 % destruction from ThT fluorescence is observed), and 1:5 (where fibril destruction is higher than 70 %) were chosen for next analyses. These concentrations are highlighted in the Fig. 4a. The effect on protein amyloid destruction has been only partially investigated. Barros et al. showed that the addition of Au-NPs to lysozyme fibrils was associated with a larger amount of β -sheet structures in the system once equilibrium was reached [55].

2.2.3. Effect of MNPs/aaMNPs on zeta potential of α LA and LAF

Understanding the variations in the zeta potential of nanoparticles as they bind with protein species during amyloid fibrillization is crucial for unraveling the potential inhibitory mechanisms of aaMNPs. Structural changes in α LA monomers and different amyloid species upon NP binding can alter electrostatic interactions, thereby affecting zeta potential [56]. Zeta potential measurements were conducted for aaMNPs at two concentrations (Table S1b) and α LA+MNPs/aaMNPs mixtures at 1:1 and 1:5 ratios before and after incubation (Fig. 2b). The zeta potential of certain nanoparticles alone (MNPs, PLLMNPs, and ProMNPs) remained consistent with increasing concentration, while others showed an increase, notably CysMNPs. Upon incubation with α LA, certain nanoparticles exhibited changes in zeta potential. α LA+MNPs, α LA+CysMNPs, and α LA+ProMNPs mixtures at a 1:1 ratio showed increased zeta potential compared to nanoparticles alone. However, at a 1:5 ratio, the charge of ProMNPs appears to influence their inhibitory activity significantly. Minimal zeta potential changes were observed for α LA+PLLMNPs. Changes in zeta potential with time were not observed for the α LA+CysMNPs complex. It agrees with its lowest inhibitory capacity. The zeta potential values of α LA and LAF confirm the influence of protein size and structure (Fig. 4b).

Complexes of LAF with MNPs, CysMNPs, PLLMNPs, and ProMNPs showed increased zeta potential compared to aaMNPs alone, Fig. 4b. The zeta potential of native α -lactalbumin (α LA) and LAF was 18.1 mV and 38.4 mV, respectively. Minimal zeta potential changes were observed with increasing MNPs/aaMNPs concentration, with a more pronounced increase for CysMNPs. Zeta potentials of LAF: MNPs/aaMNPs complexes remained relatively stable over 24 hours at both aaMNPs concentrations (no significant zeta potential change was noted). This suggests that the charge of aaMNPs may not influence their depolymerization activity under these conditions.

To better understand anti-amyloid effects of MNPs/aaMNPs, additional studies utilizing FTIR and AFM will concentrate only on aaMNPs and their influence on α LA aggregation.

2.3. Activity of aaMNPs on α Lactalbumin aggregation - AFM morphological analysis

2.3.1. AFM morphological analysis for depolymerization

AFM is an essential technique for the study of surfaces and their interactions, especially in the case of bio-/non-bio- interfaces. AFM has been used to visualize the impact of aaMNPs on mature LAF at various concentration ratios selected from DC_{50} curves. Figure S3 displays typical AFM images of LAF incubated with CysMNPs, PLLMNPs, and ProMNPs at LAF:aaMNPs ratios of 10:1, 1:1, and 1:5. In the 10:1 ratio, NPs are barely visible. In contrast, in the 1:5 ratio, their abundance obscures fibril characterization. Further analysis focused on the 1:1

ratio, optimal for distinguishing between fibrils and nanoparticles. AFM images in Fig. 5a show a reduction in amyloid fibrils, confirming the destroying activity of each aaMNPs type. Interaction between LAF and aaMNPs leads to fibril destruction, forming diverse complexes evidenced by increased number of small objects on the mica surface.

AFM images underwent statistical analysis to quantify aaMNPs' destroying activity and characterize LAF morphology. Detailed analysis procedures are outlined in Section 4.4. Grains on the AFM image for LAF+CysMNPs, for example, were separated based on minimum circumferential radius (R_c) into two intervals: below 100 nm (small R_c) and above 100 nm (big R_c) (Fig. 5b). This categorization aimed to distinguish nanoparticles from longer fibrillar objects. Circularities and analyzed grain numbers are reported.

The diameter of these complexes represents their size in one dimension while considering their overall size in three dimensions requires the calculation of the volume. Therefore, we conducted calculations to determine the volume as a function of the objects' diameters in all AFM images. This analysis provides valuable insights into the size and morphology of the complexes formed between LAF and aaMNPs, elucidating the nature of their interactions and the effects on amyloid fibril structure.

Histograms of grains' volume per $1 \mu\text{m}^2$ for both intervals are shown in Fig. 5c for LAF alone (grey bars), aaMNPs alone (semi-transparent wide bars), and LAF+aaMNPs mixtures (full colored bars). The minimum volume between the grain surface and the plane $z = z_{\min}$, where z_{\min} is the minimum height present in the grain, was calculated for each grain. Errors were estimated as the root sum of the statistical uncertainties (maximum semi-dispersion).

The provided discussion focuses on the analysis of objects in AFM images, particularly concerning different ranges of diameters. It is important to notice the number of objects observed. In the range of small R_c for only aaMNPs, thousands of objects are present on images (2500–4500 objects were analyzed); for complexes LAF+aaMNPs within the small diameter range, the number of observed objects is significantly lower. We found only tens of objects, with the analysis ranging from 3.5 to 100. The number of objects observed increases when examining a larger range of diameters for the same complexes LAF+aaMNPs. In this case, we observed hundreds to thousands of objects in the images, with the analysis ranging from 100 to 1500.

Histograms show small objects (small R_c) are nearly absent in the case of LAF alone (control). In the small R_c range, an increased volume has been noted in the case of LAF+CysMNPs, which is in good agreement with its lowest DC_{50} value. A decreased volume for LAF+PLLMNPs, compared to CysMNPs and PLLMNPs alone, is observed. In the case of the LAF+ProMNPs complex, the volume remains almost unchanged. In the large R_c range, the average object volume remains unchanged for all LAF+aaMNPs mixtures compared to LAF alone, but the number of objects is different. For only LAF hundreds of objects were observed compared to, complexes LAF+aaMNPs resulting in thousands of objects, but evidently shorter. These findings suggest different effects of aaMNPs on the size and morphology of amyloid fibrils after 24 h incubation, particularly in the small R_c range. At the same time, minimal alterations are observed in the big R_c range.

We plotted the collected data for each LAF+aaMNPs mixture alongside LAF and aaMNPs alone to analyze grain volume values against their diameter. Using the LAF+CysMNPs mixture as an example (Figure S4a), objects within a 1000 nm diameter range are presented to illustrate the relationship between volume and diameter. The data for only LAF and only CysMNPs were fitted with an exponential function. This exponential relationship showed that as the diameter increased, the volume grew more rapidly for only CysMNPs compared to only LAF (twice). In Figure S4b, the volume values vs diameter is shown in a logarithmic scale. Linear regression was used to derive the slope, indicating the rate of volume change concerning diameter for each population (LAF, CysMNPs, and their complex) within the 50–3000 nm diameter range (Figure S4c). Contributions of three populations are

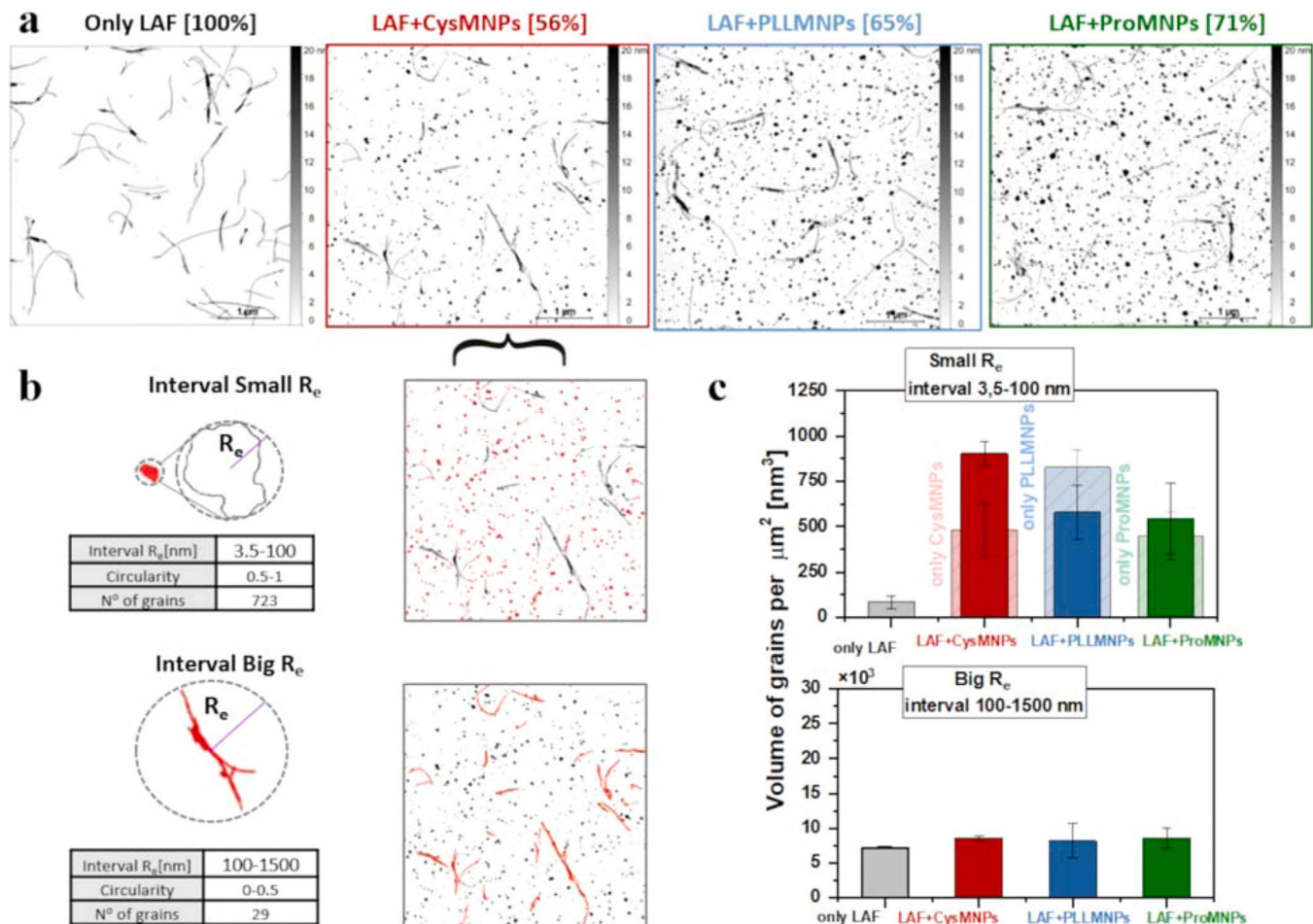


Fig. 5. a) Typical AFM images of 7 $\mu\text{g}.\text{ml}^{-1}$ LAF alone and in the presence of aaMNPs after 24 h incubation at 37 °C: from left to right LAF alone (control), LAF+CysMNPs, LAF+PLL MNPs and LAF+ProMNPs. The ratio of LAF:aaMNPs = 1:1. All images are 5×5 μm with a scale bar representing 1 μm . b) Grain selections from LAF+CysMNPs AFM image; grains are separated in two intervals of the minimum circumcircle radius R_e : below 100 nm (small R_e interval) and above 100 nm (big R_e interval). Grain circularity corresponds to 0.5–1 for a small interval and 0–0.5 for a big one. c) The surface volume of grains per 1 μm^2 for adequate intervals is plotted. The errors were estimated as the sum in quadrature of statistical uncertainties (maximum semi-dispersion). Semi-transparent bars represent aa-MNPs alone.

evident.

We repeated this analysis for every LAF+aaMNPs mixture and found that each mixture exhibited a higher packing density than LAF alone (higher slope values), indicating aaMNPs' affinity to LAF, see Figure S5. For mature LAF, we observe fibrils maximum diameter/length of up to 3 000 nm. This is in good agreement with published data [57]. For LAF+aaMNPs complexes, this value is significantly reduced, reaching a maximum of 1 500–1 800 nm, resulting in shorter and more compact aggregates. However, the slope values for mixtures were lower compared to aaMNPs alone, suggesting a less densely packed structure. This indicates that the 24 h treatment of LAF with aaMNPs resulted in the presence of a significant quantity of smaller objects compared to only LAF, confirming the destructive effect of aaMNPs. All derived values are listed in Table S2.

Our depolymerization study shows that aaMNPs have the ability to depolymerize LAF to some extent in concentration-dependent manner. However, the surface functionalization of aaMNPs has no significant impact on the observed depolymerization activity of aaMNPs (DC_{50} values within the range of 190 – 275 $\mu\text{g}.\text{ml}^{-1}$). AFM images analysis suggest that morphological changes in LAF+aaMNPs complexes, especially in small intervals of diameters, indicate potential interactions facilitating depolymerization.

We suggest that the ability of aaMNPs to destroy LAF is caused by the adsorption of the nanoparticles on amyloid fibrils. A similar effect was observed for the interaction of MNPs with amyloid fibrils of hen egg

white lysozyme [58]. The interactions between nanoparticles and fibrils most likely lead to the interruption of the interface between two neighboring β -sheets stabilizing the amyloid fibrils. These results are in good agreement with published data regarding the destroying activity of various nanoparticles [46,50].

2.3.2. AFM morphological analysis for inhibition

It's crucial to highlight the complementary nature of ThT fluorescence and AFM imaging in characterizing fibril formation processes. AFM images of αLA amyloid structures formed alone or with aaMNPs (at 1:1 concentration ratio) reveal crucial insights, Fig. 6. At 25 minutes, αLA alone displays short protofibrils and fibrillar aggregates, progressing to longer, mature fibrils at 180 minutes. In contrast, αLA with CysMNPs at 25 minutes exhibits small objects, likely nanoparticles with protein prefibrillar species, and short protofibrils. By 180 minutes, mature fibrils with fewer free nanoparticles are observed. Similarly, αLA with ProMNPs at 25 minutes shows significant material deposition, mainly protofibrils or prefibrillar species, and short fibrils. By 180 minutes, shorter fibrils and aggregates, distinct from untreated fibrils, are present. The αLA +PLL MNPs complex, with the longest lag time, predominantly reveals small non-fibrillar objects at 25 minutes, transitioning to short mature fibrils at 180 minutes. These observations underscore the significant impact of all aaMNPs on fibril formation dynamics, highlighting the interplay between nanoparticles, fibril assembly rates, and resultant fibril morphology.

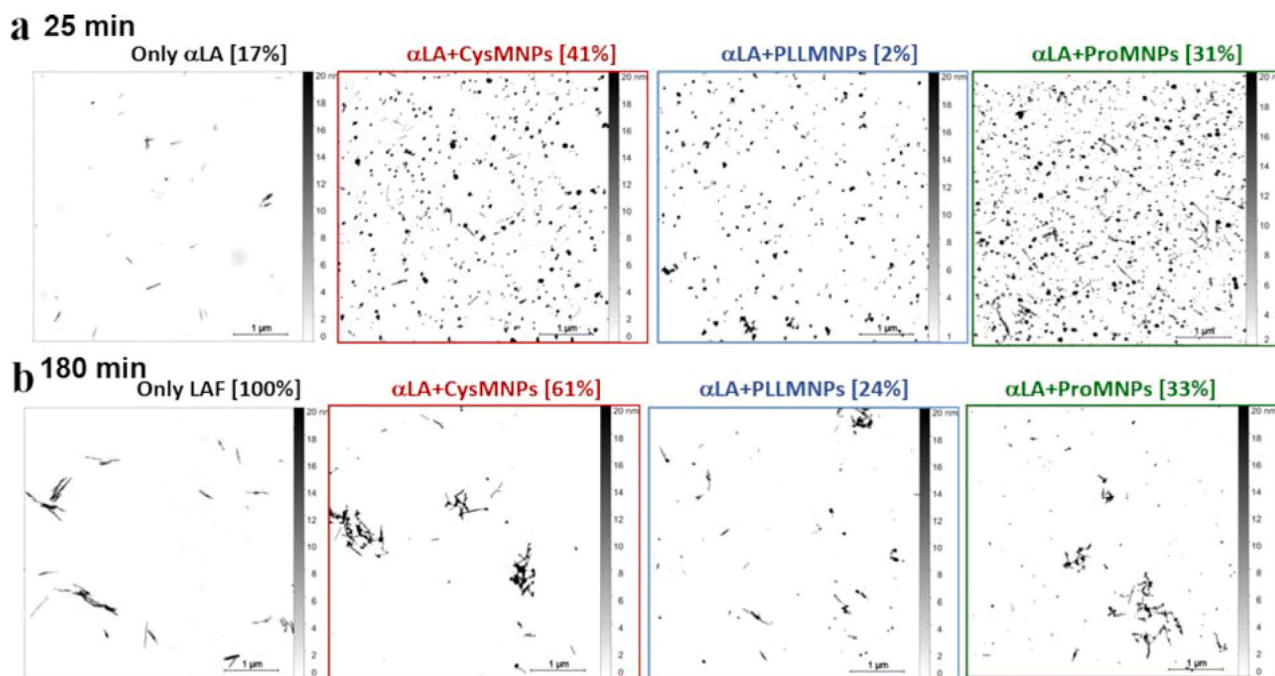


Fig. 6. Typical AFM images of $7 \mu\text{g.ml}^{-1}$ αLA amyloid structures formed alone and in the presence of aaMNPs measured after **a)** 25 min and **b)** 180 min at 65°C and 1200 rpm: from left to right CysMNPs, PLLMNPs and ProMNPs. The ratio of αLA : aaMNPs = 1:1. All images are $5 \times 5 \mu\text{m}$ with a scale bar representing $1 \mu\text{m}$. Percentage taken from measurement of relative ThT fluorescence.

Statistical analyses of samples post-inhibition experiments further elucidate these dynamics. The diameter/length of fibrils in complexes with aaMNPs is significantly reduced compared to untreated fibrils, resulting in shorter and more compact aggregates. Notably, the slopes of observed populations of complexes remain relatively consistent over time, suggesting sustained interactions within complexes, Figure S6.

The histograms of object volume per μm^2 , showed in Fig. 7, reveal fluctuations over time, with smaller objects dominating initially, especially in complexes of CysMNPs and ProMNPs, indicating accelerated nucleation processes. However, after 180 minutes, all αLA +aaMNPs complexes exhibit an abundance of objects, with significant increases in volume observed in the larger size range, coinciding with changes in

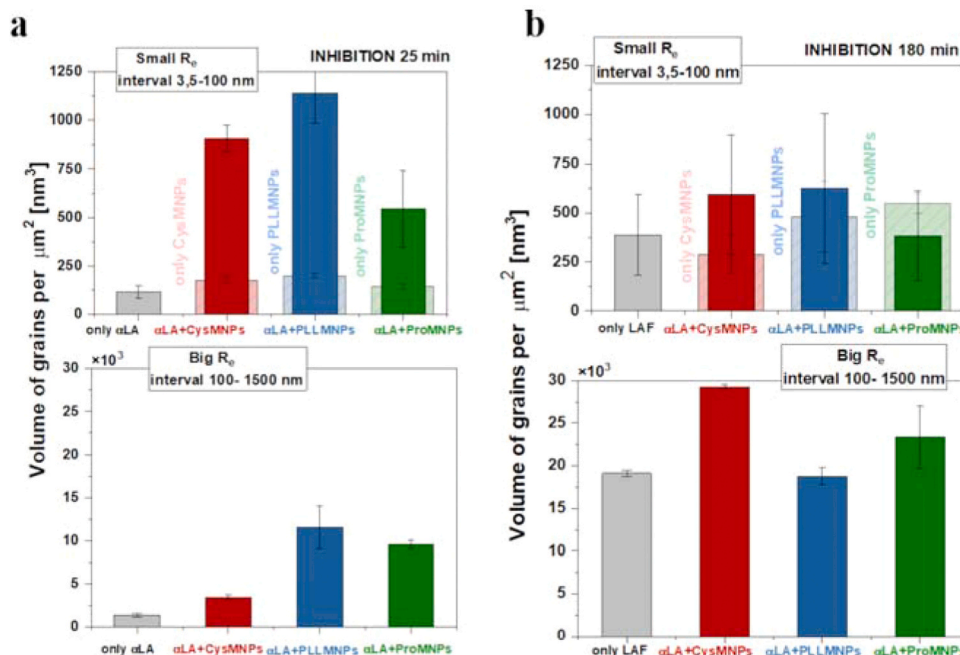


Fig. 7. Statistical analyses from AFM images. Bar graphs depicting the volume of grains in the population of objects per square micrometer (μm^2) under inhibition conditions at two specific time points: **a)** 25 minutes and **b)** 180 minutes. Histograms depict the distribution of objects in both large and small size ranges. At 25 minutes, small objects ($< 100 \text{ nm}$) are prevalent (Small R_g range), contrasting with a scarcity of objects above 100 nm (Big R_g), notably in αLA . However, by 180 minutes, histograms balance in both intervals. There's a tripling of objects in Big R_g ranges. The use of two distinct time points implies a temporal aspect to the study and provides insights into the dynamics of the inhibition process over time.

zeta potential. The longer lag phase in α LA+PLLMNPs contributes to higher volumes of objects, reflecting the relationship between lag phase duration and object volume.

The relative ThT fluorescence percentage values serve as indicators of amyloid fibril presence and abundance in relation to observed object volumes. Despite representing 100 % fibrils, untreated α LA exhibits volume distributions similar to those of α LA+PLLMNPs and α LA+ProMNPs after 180 minutes. This comprehensive overview highlights the intricate dynamics of object distribution over time and the influence of amino acid coatings on object density and behaviour in the studied systems.

In conclusion, the integration of ThT fluorescence and AFM provides a holistic understanding of protein fibril formation processes, especially in the presence of aaMNPs. These techniques reveal crucial insights into fibril morphology, nanoparticle-protein interactions, and the dynamics of fibril assembly.

2.4. Activity of aaMNPs on α Lactalbumin secondary structure - FTIR analysis

ATR-FTIR spectroscopy was utilized to analyze the secondary structure of α LA after inhibition and destruction by aaMNPs at a 1:1 ratio, Fig. 8. Deconvolution of the spectra obtained after inhibition revealed a shift in absorption maxima, indicating a reduction in β -sheet content by almost 30 % compared to untreated α -LA fibrils (Table S5). This suggests the ability of aaMNPs to inhibit amyloid aggregation, which is consistent with ThT assay and AFM findings. The position of the bands in the amide I region provides information about the secondary structure of the aggregates. Mature LAF (control) are characterized by 1617 cm^{-1} , 1624 cm^{-1} , and 1636 cm^{-1} bands, indicating a significant amount of β -sheet secondary structure typical for amyloid fibrils [59].

The spectra of all LAF+aaMNP mixtures contain these bands; however, a decrease in intensity was observed. Our data show that, compared to LAF alone, LAF+aaMNPs shifted absorption maxima from 1624 cm^{-1} towards 1646 cm^{-1} , indicating an increase of unordered structure at the expense of β -sheets supporting the ability of aaMNPs to depolymerize LAF to some extent. Deconvolution of the recorded spectra was performed to quantify the protein secondary structure content, which is summarized in Table S3.

3. Conclusions

Our study demonstrates the dose-dependent effect of uncoated MNPs and aaMNPs on the process of α LA amyloid fibrils formation and mature LAF destruction. ProMNPs, with smaller hydrodynamic diameter, showed the most potent inhibitory effect ($\text{IC}_{50}=134.6 \mu\text{g}.\text{ml}^{-1}$), while CysMNPs displayed the strongest depolymerizing efficiency ($\text{DC}_{50} = 190.4 \mu\text{g}.\text{ml}^{-1}$).

The incubation of aaMNPs with LAF destabilizes and destroys the LAF. Nanoparticles provide a large surface area for interactions with LAF, facilitating the destabilization of LAF β -sheets. This leads to the formation of amyloid aggregates with a higher content of unordered structures at the expense of β -structures.

In the inhibition scenario, aaMNPs adsorbed protein monomers, reducing the availability of free monomers to aggregate, resulting in fewer fibrils. Interestingly, ProMNPs possess dual inhibitory activity. They can bind monomers and prefibrillar species, leading to the decrease of free monomers and facilitate the formation of short-lifetime oligomers, accelerating the formation of low amounts of amyloid fibrils.

AFM imaging revealed alterations in aggregate morphology upon interaction with aaMNPs, influencing fibril size distribution. For the first time, statistical analysis of AFM images quantified the anti-amyloid

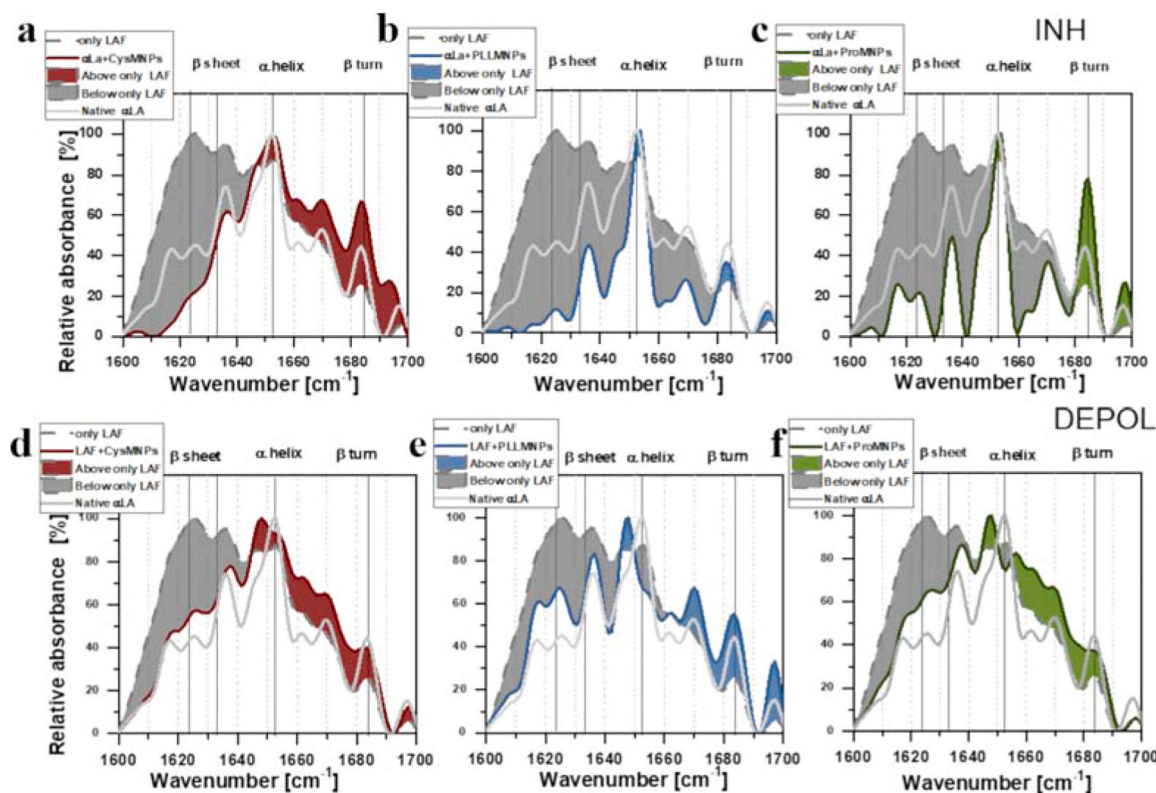


Fig. 8. ATR-FTIR spectra recorded to determine inhibition (a-c) and depolymerization (d-f) activity of aaMNPs on secondary structure of α LA aggregates. FTIR spectra of native α Lactalbumin (α LA; full light grey lines), untreated LAF (only LAF; dashed dark grey lines) and after 3 h of fibrillization of α LA in the presence of aaMNPs: a) α LA+CysMNPs (red solid line), b) α LA+PLLMNPs (blue solid line) and c) α LA+ProMNPs (green solid line) and after 24 h incubation of mature fibrils with aaMNPs: d) LAF+CysMNPs (red solid line), e) LAF+PLLMNPs (blue solid line) and f) LAF+ ProMNPs (green solid line).

activity of aaMNP, demonstrating their influence on the dimensionality of amyloid aggregates. AFM analysis provided insights at the nanoscale level, enhancing our understanding of nanoparticle-fibril complexes.

Moreover, differences in cytotoxicity observed between PLLMNP, CysMNP, and ProMNP may stem from variations in their surface properties. While CysMNP and ProMNP showed minimal cytotoxicity, PLLMNP induced cell death, and altered morphology, likely due to their high positive charge density. In summary, our findings indicate that the coating and size of nanoparticles are very important in influencing amyloid aggregation.

These findings suggest diverse mechanisms of aaMNP's anti-amyloid effect and help understand the impact of different surface modifications on protein amyloid aggregation.

4. Experimental methods

Poly-L-lysine hydrobromide (0.1 % (w/v) in H₂O, Mw = 150000 – 300000 g/mol), L-proline (99 %), cysteine (≥ 98 %), ferric chloride hexahydrate (FeCl₃·6 H₂O), ferrous sulfate heptahydrate (FeSO₄·7 H₂O), ammonium hydroxide (NH₄OH), perchloric acid (HClO₄), α -lactalbumin from bovine milk (lyophilized powder, type III, calcium depleted, purity ≥ 85 %, lot number L6010, CaCl₂, thioflavin T (ThT) and all other chemicals were obtained from Sigma-Aldrich Company (St. Louis, MO). The protein concentrations were determined spectrophotometrically (UV VIS JASCO V-630 spectrophotometer) using an extinction coefficient for α -lactalbumin in water (ϵ) of 28,540 M⁻¹ cm⁻¹ at 280 nm at $\lambda = 280$ nm [60]. Ultrapure deionized water (Milli-Q) was used throughout the experiments.

4.1. Preparation of iron oxide nanoparticles

Aqueous solution of magnetic nanoparticles (MNP) stabilized with perchloric acid was prepared by the method described in detail previously [28,29]. The concentration of Fe₃O₄ in MNP estimated by thiocyanate colorimetry [61] was 30 mg. ml⁻¹. The coating of iron oxide MNP with amino acid (aa) cysteine (Cys), poly-L-lysine (PLL) or proline (Pro) was carried out by mixing aqueous solution of the corresponding amino acid with MNP in the weight ratio of aa/Fe₃O₄ = 1.3/1, 2/1 and 5/1 for Cys, PLL and Pro, respectively. Then, the samples were centrifuged at 35 000 rpm for 2 hours; the nonmagnetic fraction (supernatant) was removed. The sediment (magnetic fraction) containing Fe₃O₄ at concentration of 20 mg. ml⁻¹ (determined by colorimetric method) was used for further experiments and are referred to as aaMNP.

4.2. Dynamic light scattering method (DLS) and Laser Doppler velocimetry of iron oxide nanoparticles

The prepared samples were characterized using a various method in order to determine their properties.

Zetasizer NanoZS (Malvern Instruments) instrument was used for both particle size analysis (using DLS as the basic principle of operation) and zeta-potential measurement (using Doppler electrophoresis as the basic principle of operation). DLS with laser beam $\lambda = 633$ nm produced by a He-Ne laser, operating with a scattering angle of 173°, was applied to determine the hydrodynamic size distribution of MNP and aaMNP. The measuring cell (DTS0012) was used for the size determination studies. Electrophoretic mobility was measured using a Folded Capillary Zeta Cell (DTS1070). The samples with the desired concentration were injected into the cells to cover the electrodes of the cells completely. The sample was injected slowly into the cells to avoid air bubbles, and analysis was only carried out if no visible air bubble inclusions were present. After measurements, the instrument calculated the zeta potential from the electrophoretic mobility using the Smoluchowski equation: $\zeta = (U \cdot \eta / \epsilon)$, where ζ is zeta potential, U is electrophoretic mobility, η is a medium viscosity, and ϵ is the dielectric constant. The zeta potential transfer standard from Malvern was used for instrument

verification.

4.3. ATR-FTIR spectroscopy of aaMNP

ATR-FTIR spectra of 30 mg. ml⁻¹ amino acids, 10 mg. ml⁻¹ aaMNP alone were recorded with a Nicolet 8700 FTIR spectrometer (Thermo Scientific) equipped with a Smart OMNIC sampler (diamond prism). Each spectrum represents an average of 64 interferograms recorded in the broad region (1800–500 cm⁻¹) with a resolution of 4 cm⁻¹. Each sample was measured as a triplicate ($n = 3$). The buffer (background) was subtracted from the spectrum.

4.4. AFM measurements

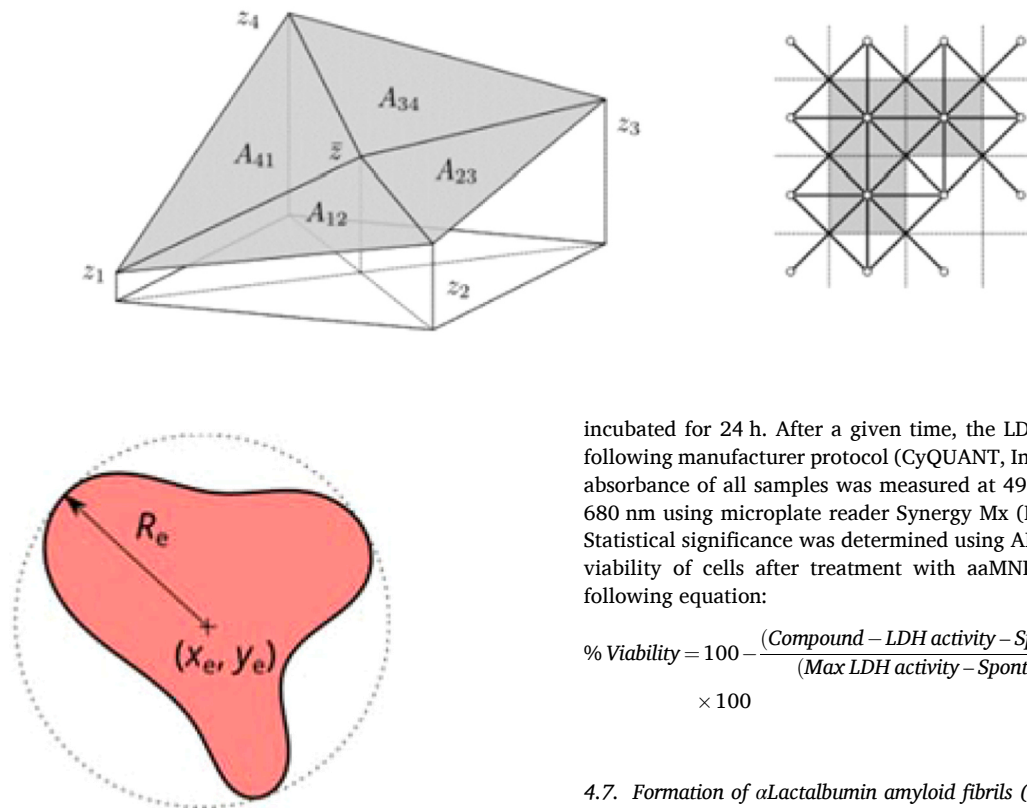
Samples of aaMNP, and LAF+aaMNP, α LA+aaMNP complexes for AFM were prepared by drop casting method. An aliquot of 10 μ L solution diluted to a required concentration was deposited on the surface of freshly cleaved mica and after 10 min adsorption, the substrate was rinsed with ultrapure water and dried with N₂ gas. AFM images were taken in the SPM@ISMN facility using a standalone SMENA NT-MDT (NT-MDT, PRA.MA. Sondalo, Italy) microscope operated in semi-contact mode by silicon cantilevers (NSG10, NT-MDT, PRA.MA. Sondalo, Italy) with typical force constant 11.8 N/m. The topographic images were corrected line by line for background trend effect with second-order polynomial fitting (Image Analysis 2.2.0, NT-MDT, PRA.MA. Sondalo, Italy) and line profile analyses were performed using Gwyddion software [62].

4.5. Analysis of AFM- data processing and grain analysis

All images for statistical analyses were 5 μ m x 5 μ m in size with resolution set to 1024 x 1024 px². This means that 1 pixel corresponds to 4.88 nm. This is an important factor to take into consideration since we worked with nanoparticles with diameters of tens of nanometers and considering that the tip has a radius of curvature of 10 nm, a pixel resolution allows us to describe nanoparticles with more pixels (i.e. with more points). All images were analyzed with Gwyddion software [62], an open source software dedicated to the analysis of images produced with microscopes probe scanning. Overall 2500–4500 objects were analyzed.

To be able to distinguish and analyze nanoparticles, single or more frequently aggregated, from protofibrils or mature fibrils we used two parameters: I.) *Circularity* - this parameter is calculated as a function of a circumference which has the same area as the object and the perimeter of the particle projected. The value of roundness, between 0 and 1, allows us to do so to evaluate the geometry of an object; a perfectly rounded object will assume circularity equal to 1 while an object completely irregular will assume circularity equal to 0. On the basis of this parameter, in our study we hypothesized that we could do this classification: protofibrils or mature fibrils were marked as objects with circularity between 0 and 0.5, i.e. as multiple objects or less irregular while the nanoparticles were marked as objects with circularity between 0.5 and 1, i.e. as regular objects (rounded). II.) Minimum circumscribed radius ("R_e"): corresponds to the radius of the smallest circumference containing the object [63]:

Nanoparticles are objects much smaller than the fibrils and taking the phenomenon into account of tip-sample convolution, it was possible to group the nanoparticles in the R_e range 0–100 nm (Interval small R_e) and the fibrils in the range R_e 100–1500 nm (Interval big R_e). We have these values subsequently doubled to obtain the diameter of the circumscribed minimum.



After setting these parameters, we analyzed the number of objects presented on AFM images, their area and their volume. Gwyddion offers different mathematical functions to calculate the area and volume of objects. We used the following functions: I.) "Surface area": the surface area is estimated by the following method. Let z_i for $i = 1, 2, 3, 4$ denote values in four neighbor points (pixel centers), and h_x and h_y pixel dimensions along corresponding axes. If an additional point is placed in the center of the rectangle which corresponds to the common corner of the four pixels (using the mean value of the pixels), four triangles are formed and the surface area can be approximated by summing their areas. The method is now well-defined for inner pixels of the region. The triangulation scheme for the calculation of the surface area is shown:

II) *Grain minimum basis* (V_{\min}): the volume between grain surface and the plane $z = z_{\min}$, where z_{\min} is the minimum value (height) occurring in the grain. The grain volume is, after subtracting the basis, estimated as the volume of exactly the same body whose upper surface is used for surface area calculation. Afterwards data were calculated per $1 \mu\text{m}^2$.

More than 100 images were analyzed. Each sample was measured as a triplicate. For our study, we used above described tool to export the raw data (ascii file) of the average height, surface area and volume with minimum grain base (V_{\min}). Ascii files were afterward plotted in OriginLab graphics software (OriginLab Corporation, Northampton, MA, USA) [64] with statistical test ANOVA single factor used to process the results with $p < 0.001$ ($n=3$).

4.6. Nanoparticles cytotoxicity assessment – LDH assay

The HEK 293 (human epithelial kidney cell line ATCC CRL-1573) was used to evaluate cell viability in the presence of aaMNPs. The HEK 293 cells (passage 9) were seeded to a 96-well plate at 10,000 cells/well density in 10 % DMEM and incubated overnight in a humid atmosphere (5 % CO_2 , 37 °C). The aaMNPs were firstly dispersed in ultra-pure H_2O to 10 $\text{mg}\cdot\text{ml}^{-1}$ (magnetite concentration). The serial dilution of studied NPs (0.1, 1, 10, 50, 100, and 200 $\mu\text{g}/\text{ml}$) was prepared in 10 % DMEM. The samples were added to attached cells in 96-well plates and

incubated for 24 h. After a given time, the LDH assay was performed following manufacturer protocol (CyQUANT, Invitrogen company). The absorbance of all samples was measured at 490 nm with correction at 680 nm using microplate reader Synergy Mx (BioTek Company, USA). Statistical significance was determined using ANOVA single factor. The viability of cells after treatment with aaMNPs was calculated from following equation:

$$\% \text{ Viability} = 100 - \frac{(\text{Compound} - \text{LDH activity} - \text{Spontaneous LDH activity})}{(\text{Max LDH activity} - \text{Spontaneous LDH activity})} \times 100 \quad (1)$$

4.7. Formation of α Lactalbumin amyloid fibrils (LAF) for depolymerization

α LA was dissolved to a final concentration of 5 $\text{mg}\cdot\text{ml}^{-1}$ in 100 mM CaCl_2 . Protein solutions' pH was adjusted to 2.0 by the addition of HCl. The formation of amyloid fibrils was achieved by incubating the protein solution at 65 °C and constant stirring (1200 rpm) for 90 min. The formation of amyloid fibrils was confirmed using ThT assay and atomic force microscopy (AFM).

4.8. Formation of α Lactalbumin amyloid fibrils (LAF) for inhibition

α LA was dissolved to a final concentration of 20 μM (284 $\mu\text{g}\cdot\text{ml}^{-1}$) in 100 mM CaCl_2 , pH 2.0. To produce the α LA amyloid fibrils (LAF), 50 μl of the protein solution was incubated at 65 °C and stirred constantly (1200 rpm) for 3 h. The formation of lysozyme amyloid fibrils was monitored by characteristic changes in thioflavin T fluorescence intensity (ThT assay). Morphology of fibrils was examined using atomic force microscope.

4.9. Thioflavin T (ThT) fluorescence assay

20 μM thioflavin T was added to α LA samples (10 μM) and samples were incubated at 37 °C for 1 h. Fluorescence intensity was measured in black 96-well plates using a Synergy Mx spectrofluorometer (BioTek Company, USA). The excitation wavelength was set at 440 nm, and the emission recorded at 485 nm. The emission slits were adjusted to 9.0/9.0 nm, and the top probe vertical offset was 6 mm. All ThT fluorescence experiments were performed in triplicate and the final value is the average of measured values with average deviation.

4.10. Effect of aaMNPs on α LA amyloid fibrillization and LAF-determination of IC_{50} and DC_{50}

The fibrillization of α LA was carried out in presence of CysMNPs, PLLMNPs and ProMNPs to investigate their ability to inhibit the formation of amyloid aggregates and to destroy LAF. To determine IC_{50} and DC_{50} values (concentration of nanoparticles at which inhibition of fibril

formation or destroying of amyloid fibrils is half maximal), the effect of studied nanoparticles was investigated at nanoparticle concentrations ranging from $2 \mu\text{g}.\text{ml}^{-1}$ to $4260 \mu\text{g}.\text{ml}^{-1}$ of Fe_3O_4 at a fixed protein concentration ($10 \mu\text{M}$ corresponding to $142 \mu\text{g}.\text{ml}^{-1}$ for inhibition experiments and $20 \mu\text{M}$ corresponding to $284 \mu\text{g}.\text{ml}^{-1}$ for depolymerization experiments). The extent of aggregation was observed using ThT assay. All data were normalized to ThT fluorescence determined for LAF fibrils formed alone (100 %). Each experiment was performed in 6 replicas and the final value represents the average of the measured values with average deviation. The IC_{50} and DC_{50} values were determined from curves obtained by fitting of the average fluorescence values with sigmoidal function - Sigmoid, Parameter 3 in the Origin software (Systat Software Inc., USA) using following equation

$$y = \frac{a}{\left(1 + \exp\left(\frac{(x-x_0)}{b}\right)\right)} \quad (2)$$

where x_0 corresponds to IC_{50} or DC_{50} value.

4.11. Kinetics of amyloid fibrillization

ThT assay was used for measurement of the kinetics of αLA fibril formation alone ($284 \mu\text{g}.\text{ml}^{-1}$) or in presence of aaMNP ($284 \mu\text{g}.\text{ml}^{-1}$), w/w ratio of LAF: nanoparticles (related to Fe_3O_4) = 1: 1. The samples were incubated at 65°C , acidic pH and the aliquots were withdrawn at given time. Every experiment was performed in 6 replicas and the reported values are averages of measured data, the error bars represent the average deviation.

4.12. Analysis of kinetics data of amyloid fibrillization

The kinetics of αLA fibril fibrillization represented by changing of ThT fluorescence intensities were plotted as a function of time and fitted by a Boltzmann sigmoidal described by following equation

$$y = A_1 + \frac{(A_2 - A_1)}{\left(1 + \exp\left(\frac{-(t-t_{\text{half}})}{\tau}\right)\right)} \quad (3)$$

where y is the fluorescence intensity, A_1 and A_2 are the initial and the final values of ThT fluorescence intensity, t is the time, t_{half} is the time at half-height of fluorescence maximum, and τ is the time constant describing the steepness of the curve at $t = t_{\text{half}}$. This equation was used to determine the kinetic parameters including the lag time $t_{\text{lag}} = t_{\text{half}} - 2\tau$, the apparent fibril growth rate $\frac{k_{\text{app}}-1}{\tau}$ and $\text{span} = A_2 - A_1$.

4.13. ATR-FTIR spectroscopy of αLA , LAF and their mixtures with aaMNPs

Solution of $5 \text{ mg}.\text{ml}^{-1}$ αLA , LAF, and $\alpha\text{LA}/\text{LAF}:\text{aaMNPs}$ mixtures ($5 \text{ mg}.\text{ml}^{-1}$ of $\alpha\text{Lactalbumin}$ incubated 3 h for inhibitory experiment, 24 h for destroying) with $5 \text{ mg}.\text{ml}^{-1}$ studied nanoparticles) were recorded with a Nicolet 8700 FTIR spectrometer (Thermo Scientific) equipped with a Smart OMNIC sampler (diamond prism). Each spectrum represents an average of 254 interferograms recorded in the amide I region ($1700\text{--}1600 \text{ cm}^{-1}$) with a resolution of 2 cm^{-1} . Each sample was measured as a triplicate ($n = 3$). The buffer (background) was subtracted from the spectrum.

CRediT authorship contribution statement

Zuzana Gazova: Writing – review & editing, Validation, Supervision, Resources, Funding acquisition, Conceptualization. **Andrea Antosova:** Writing – review & editing, Writing – original draft, Validation, Supervision, Methodology, Investigation, Funding acquisition,

Formal analysis, Data curation, Conceptualization. **Barbara Luppi:** Writing – original draft, Data curation. **Eva Bystrenova:** Writing – review & editing, Writing – original draft, Visualization, Validation, Supervision, Methodology, Investigation, Funding acquisition, Formal analysis, Data curation, Conceptualization. **Patrizio Graziosi:** Writing – original draft, Funding acquisition. **Vlasta Zavisova:** Writing – original draft, Funding acquisition. **Martina Koneracka:** Writing – original draft, Resources, Funding acquisition. **Olga Parmar:** Investigation. **Patrizia Verducci:** Investigation, Formal analysis, Data curation. **Iryna Antal:** Writing – original draft, Investigation, Data curation. **Martina Kubovcikova:** Investigation, Funding acquisition, Data curation. **Zuzana Bednarikova:** Writing – review & editing, Writing – original draft, Methodology, Data curation, Conceptualization. **Miroslav Gancar:** Writing – original draft, Formal analysis, Data curation.

Declaration of Competing Interest

The authors declare the following financial interests/personal relationships which may be considered as potential competing interests, Eva Bystrenova reports financial support was provided by Institute of Nanostructured Materials National Research Council. If there are other authors, they declare that they have no known competing financial interests or personal relationships that could have appeared to influence the work reported in this paper.

Acknowledgments

This work was supported by the Slovak Research and Development Agency under the Contract no. APVV-22-0598, APVV DS-FR-22-0037; Slovak Grant Agency VEGA 02/0176/21, 2/0049/23; the Operational Program Integrated Infrastructure funded by the ERDF ITMS2014+: 313011AUW7 “NANOVIR”; and Ministry of University and Research of Italy (PRIN grant 2022SRHPF2 and PNRR grant P20227P7WZ). Microscopy was carried out at the SPM@ISMN facility.

Appendix A. Supporting information

Supplementary data associated with this article can be found in the online version at doi:10.1016/j.nanoso.2024.101413.

Data availability

Data will be made available on request.

References

- [1] F. Chiti, C.M. Dobson, Protein Misfolding, Amyloid Formation, and Human Disease: A Summary of Progress Over the Last Decade, *Annu. Rev. Biochem.* 86 (2017) 27–68, <https://doi.org/10.1146/annurev-biochem-061516-045115>.
- [2] S. Naskar, N. Gour, Realization of Amyloid-like Aggregation as a Common Cause for Pathogenesis in Diseases, *Life* 13 (2023) 1523, <https://doi.org/10.3390/life13071523>.
- [3] E. Chatani, N. Yamamoto, Recent progress on understanding the mechanisms of amyloid nucleation, *Biophys. Rev.* 10 (2018) 527–534, <https://doi.org/10.1007/s12551-017-0353-8>.
- [4] B. Lönnnerdal, E.L. Lien, Nutritional and Physiologic Significance of α -Lactalbumin in Infants, *Nutr. Rev.* 61 (2003) 295–305, <https://doi.org/10.1301/nr.2003.sept.295-305>.
- [5] E.A. Permyakov, L.J. Berliner, α -Lactalbumin: structure and function, *FEBS Lett.* 473 (2000) 269–274, [https://doi.org/10.1016/S0014-5793\(00\)01546-5](https://doi.org/10.1016/S0014-5793(00)01546-5).
- [6] D. Kuroski, W. Lauro, I.K. Lednev, Amyloid fibrils are “alive”: spontaneous refolding from one polymorph to another, *Chem. Commun.* 46 (2010) 4249, <https://doi.org/10.1039/b926758a>.
- [7] S. Giorgetti, C. Greco, P. Tortora, F.A. Aprile, Targeting Amyloid Aggregation: An Overview of Strategies and Mechanisms, *Int. J. Mol. Sci.* 19 (2018) 2677, <https://doi.org/10.3390/ijms19092677>.
- [8] P.C. Ke, E.H. Pilkington, Y. Sun, I. Javed, A. Kakinien, G. Peng, F. Ding, T.P. Davis, Mitigation of Amyloidosis with Nanomaterials, *Adv. Mater.* 32 (2020), <https://doi.org/10.1002/adma.201901690>.
- [9] M. Mahmoudi, O. Akhavan, M. Ghavami, F. Rezaee, S.M.A. Ghiasi, Graphene oxide strongly inhibits amyloid beta fibrillation, *Nanoscale* 4 (2012) 7322, <https://doi.org/10.1039/c2nr31657a>.

- [10] A. Gladysz, B. Abel, H.J. Risselada, Gold-Induced Fibril Growth: The Mechanism of Surface-Facilitated Amyloid Aggregation, *Angew. Chem. Int. Ed.* 55 (2016) 11242–11246, <https://doi.org/10.1002/anie.201605151>.
- [11] M. Wang, Y. Sun, X. Cao, G. Peng, I. Javed, A. Kakinen, T.P. Davis, S. Lin, J. Liu, F. Ding, P.C. Ke, Graphene quantum dots against human IAPP aggregation and toxicity *in vivo*, *Nanoscale* 10 (2018) 19995–20006, <https://doi.org/10.1039/C8NR07180B>.
- [12] N. Gao, H. Sun, K. Dong, J. Ren, T. Duan, C. Xu, X. Qu, Transition-metal-substituted polyoxometalate derivatives as functional anti-amyloid agents for Alzheimer's disease, *Nat. Commun.* 5 (2014) 3422, <https://doi.org/10.1038/ncomms4422>.
- [13] N. Andrikopoulos, Z. Song, X. Wan, A.M. Douek, I. Javed, C. Fu, Y. Xing, F. Xin, Y. Li, A. Kakinen, K. Koppel, R. Qiao, A.K. Whittaker, J. Kaslin, T.P. Davis, Y. Song, F. Ding, P.C. Ke, Inhibition of Amyloid Aggregation and Toxicity with Janus Iron Oxide Nanoparticles, *Chem. Mater.* 33 (2021) 6484–6500, <https://doi.org/10.1021/acs.chemmater.1c01947>.
- [14] T. John, A. Gladysz, C. Kubeil, L.L. Martin, H.J. Risselada, B. Abel, Impact of nanoparticles on amyloid peptide and protein aggregation: a review with a focus on gold nanoparticles, *Nanoscale* 10 (2018) 20894–20913, <https://doi.org/10.1039/C8NR04506B>.
- [15] H. Mohammad-Beigi, A. Hosseini, M. Adeli, M.R. Ejtehadi, G. Christiansen, C. Sahin, Z. Tu, M. Tavakoli, A. Dilmaghani-Marand, I. Nabipour, F. Farzadfar, D. Otzen, M. Mahmoudi, M.J. Hajipour, Mechanistic Understanding of the Interactions between Nano-Objects with Different Surface Properties and α -Synuclein, *ACS Nano* 13 (2019) 3243–3256, <https://doi.org/10.1021/acsnano.8b08983>.
- [16] M. Mahmoudi, F. Quinlan-Pluck, M.P. Monopoli, S. Sheibani, H. Vali, K.A. Dawson, I. Lynch, Influence of the Physicochemical Properties of Superparamagnetic Iron Oxide Nanoparticles on Amyloid β Protein Fibrillation in Solution, *ACS Chem. Neurosci.* 4 (2013) 475–485, <https://doi.org/10.1021/cn300196n>.
- [17] C. Cabaleiro-Lago, F. Quinlan-Pluck, I. Lynch, S. Lindman, A.M. Minogue, E. Thulin, D.M. Walsh, K.A. Dawson, S. Linse, Inhibition of Amyloid β Protein Fibrillation by Polymeric Nanoparticles, *J. Am. Chem. Soc.* 130 (2008) 15437–15443, <https://doi.org/10.1021/ja8041806>.
- [18] M. Tsoli, H. Kuhn, W. Brandau, H. Esche, G. Schmid, Cellular Uptake and Toxicity of Au₅₅ Clusters, *Small* 1 (2005) 841–844, <https://doi.org/10.1002/sml.200500104>.
- [19] J.Y. Choi, S.H. Lee, H. Bin Na, K. An, T. Hyeon, T.S. Seo, In vitro cytotoxicity screening of water-dispersible metal oxide nanoparticles in human cell lines, *Bioprocess Biosyst. Eng.* 33 (2010) 21–30, <https://doi.org/10.1007/s00449-009-0354-5>.
- [20] A.K. Gupta, M. Gupta, Cytotoxicity suppression and cellular uptake enhancement of surface modified magnetic nanoparticles, *Biomaterials* 26 (2005) 1565–1573, <https://doi.org/10.1016/j.biomaterials.2004.05.022>.
- [21] H. Yin, H.P. Too, G.M. Chow, The effects of particle size and surface coating on the cytotoxicity of nickel ferrite, *Biomaterials* 26 (2005) 5818–5826, <https://doi.org/10.1016/j.biomaterials.2005.02.036>.
- [22] C. Cabaleiro-Lago, O. Szczepankiewicz, S. Linse, The Effect of Nanoparticles on Amyloid Aggregation Depends on the Protein Stability and Intrinsic Aggregation Rate, *Langmuir* 28 (2012) 1852–1857, <https://doi.org/10.1021/la203078w>.
- [23] K. Dubey, B.G. Anand, R. Badhwar, G. Bagler, P.N. Navya, H.K. Daima, K. Kar, Tyrosine- and tryptophan-coated gold nanoparticles inhibit amyloid aggregation of insulin, *Amino Acids* 47 (2015) 2551–2560, <https://doi.org/10.1007/s00726-015-2046-6>.
- [24] N. Pradhan, N.R. Jana, N.R. Jana, Inhibition of Protein Aggregation by Iron Oxide Nanoparticles Conjugated with Glutamine- and Proline-Based Osmolytes, *ACS Appl. Nano Mater.* 1 (2018) 1094–1103, <https://doi.org/10.1021/acsnano.7b00245>.
- [25] A. Antosova, Z. Bednarikova, M. Koneracka, I. Antal, J. Marek, M. Kubovcikova, V. Zavisova, A. Jurikova, Z. Gazova, Amino Acid Functionalized Superparamagnetic Nanoparticles Inhibit Lysozyme Amyloid Fibrillization, *Chem. – A Eur. J.* 25 (2019) 7501–7514, <https://doi.org/10.1002/chem.201806262>.
- [26] M. Timko, M. Koneracka, P. Kopskany, Z. Tomori, L. Vekas, A. Jozefczak, A. Skumiel, A. Radenovic, G. Dietler, E. Bystronova, M. Lita, Complex characterization of physiology solution based magnetic fluid, *Indian J. Eng. Mater. Sci.* 11 (2004) 276–282. (<http://nopr.niscares.in/handle/123456789/9290>) (accessed October 8, 2024).
- [27] A. Antosova, M. Gancar, Z. Bednarikova, J. Marek, E. Bystronova, Z. Gazova, The influence of cations on α -lactalbumin amyloid aggregation, *JBIC J. Biol. Inorg. Chem.* 27 (2022) 679–689, <https://doi.org/10.1007/s00775-022-01962-3>.
- [28] R. Massart, Preparation of aqueous magnetic liquids in alkaline and acidic media, *IEEE Trans. Magn.* 17 (1981) 1247–1248, <https://doi.org/10.1109/TMAG.1981.1061188>.
- [29] I. Antal, M. Koneracka, M. Kubovcikova, V. Zavisova, I. Khmara, D. Lucanska, L. Jelenska, I. Vidlickova, M. Zatovicova, S. Pastorekova, N. Bugarova, M. Micusik, M. Omastova, P. Kopskany, D,L-lysine functionalized Fe₃O₄ nanoparticles for detection of cancer cells, *Colloids Surf. B Biointerfaces* 163 (2018) 236–245, <https://doi.org/10.1016/j.colsurfb.2017.12.022>.
- [30] S. Honary, F. Zahir, Effect of zeta potential on the properties of nano-drug delivery systems - a review (Part 1), *Trop. J. Pharm. Res.* 12 (2013), <https://doi.org/10.4314/tjpr.v12i2.19>.
- [31] N. Malhotra, J.S. Lee, R.A.D. Liman, J.M.S. Ruallo, O.B. Villaflore, T.R. Ger, C. Der Hsiao, Potential Toxicity of Iron Oxide Magnetic Nanoparticles: A Review, 2020, Vol. 25, Page 3159, *Molecules* 25 (2020) 3159, <https://doi.org/10.3390/MOLECULES25143159>.
- [32] M. Barbalinardo, A. Antosova, M. Gambucci, Z. Bednarikova, C. Albonetti, F. Valle, P. Sassi, L. Latterini, Z. Gazova, E. Bystronova, Effect of metallic nanoparticles on amyloid fibrils and their influence to neural cell toxicity, *Nano Res* 13 (2020) 1081–1089, <https://doi.org/10.1007/S12274-020-2748-2/METRICS>.
- [33] E. Bystronova, Z. Bednarikova, M. Barbalinardo, C. Albonetti, F. Valle, Z. Gazova, Amyloid fragments and their toxicity on neural cells, *Regen. Biomater.* 6 (2019) 121–127, <https://doi.org/10.1093/rb/rbz007>.
- [34] E. Bystronova, Z. Bednarikova, M. Barbalinardo, F. Valle, Z. Gazova, F. Biscarini, Insulin amyloid structures and their influence on neural cells, *Colloids Surf. B Biointerfaces* 161 (2018) 177–182, <https://doi.org/10.1016/j.colsurfb.2017.10.054>.
- [35] H. Nosrati, N. Rashidi, H. Danafar, H.K. Manjili, Anticancer Activity of Tamoxifen Loaded Tyrosine Decorated Biocompatible Fe₃O₄ Magnetic Nanoparticles Against Breast Cancer Cell Lines, *J. Inorg. Organomet Polym. Mater.* 28 (2018) 1178–1186, <https://doi.org/10.1007/s10904-017-0758-7>.
- [36] I. Khmara, M. Koneracka, M. Kubovcikova, V. Zavisova, I. Antal, K. Csach, P. Kopskany, I. Vidlickova, L. Csaderova, S. Pastorekova, M. Zatovicova, Preparation of poly-L-lysine functionalized magnetic nanoparticles and their influence on viability of cancer cells, *J. Magn. Magn. Mater.* 427 (2017) 114–121, <https://doi.org/10.1016/j.jmmm.2016.11.014>.
- [37] S. Some, S.-M. Ho, P. Dua, E. Hwang, Y.H. Shin, H. Yoo, J.-S. Kang, D. Lee, H. Lee, Dual functions of highly potent graphene derivative–poly-L-lysine composites to inhibit bacteria and support human cells, *ACS Nano* 6 (2012) 7151–7161, <https://doi.org/10.1021/nn302215y>.
- [38] W. Liu, H.S. Choi, J.P. Zimmer, E. Tanaka, J.V. Frangioni, M. Bawendi, Compact cysteine-coated CdSe(ZnCdS) quantum dots for in vivo applications, *J. Am. Chem. Soc.* 129 (2007) 14530–14531, <https://doi.org/10.1021/ja073790m>.
- [39] F.L. de Menezes, T.M. Freire, R.R. de Castro Monteiro, R.A. Antunes, R.L.F. Melo, R.M. Freire, J.C.S. dos Santos, P.B.A. Fechine, L-cysteine-coated magnetite nanoparticles as a platform for enzymes immobilization: Amplifying biocatalytic activity of Candida antarctica Lipase A, *Mater. Res. Bull.* 177 (2024) 112882, <https://doi.org/10.1016/J.MATERRESBULL.2024.112882>.
- [40] D. Bhattacharjee, D. Sutradhar, A.K. Chandra, B. Myrbohl, L-proline as an efficient asymmetric induction catalyst in the synthesis of chromeno[2,3-d]pyrimidine-triones, xanthenes in water, *Tetrahedron* 73 (2017) 3497–3504, <https://doi.org/10.1016/j.tet.2017.05.025>.
- [41] N. Khair, R. Navas, E. Elhalel, V. Valdivia, I. Fernández, Proline-coated gold nanoparticles as a highly efficient nanocatalyst for the enantioselective direct aldol reaction in water, *RSC Adv.* 3 (2013) 3861, <https://doi.org/10.1039/c3ra22955f>.
- [42] S. Sardar, S. Pal, S. Maity, J. Chakraborty, U.C. Halder, Amyloid fibril formation by β -lactoglobulin is inhibited by gold nanoparticles, *Int. J. Biol. Macromol.* 69 (2014) 137–145, <https://doi.org/10.1016/j.ibioma.2014.05.006>.
- [43] S. Palmal, A.R. Maity, B.K. Singh, S. Basu, N.R. Jana, N.R. Jana, Inhibition of amyloid fibril growth and dissolution of amyloid fibrils by curcumin–gold nanoparticles, *Chem. – A Eur. J.* 20 (2014) 6184–6191, <https://doi.org/10.1002/chem.201400079>.
- [44] Z. Bednarikova, J. Marek, E. Demjen, S. Dutz, M.-M. Mocanu, J.W. Wu, S.S.-S. Wang, Z. Gazova, Effect of nanoparticles coated with different modifications of dextran on lysozyme amyloid aggregation, *J. Magn. Magn. Mater.* 473 (2019) 1–6, <https://doi.org/10.1016/j.jmmm.2018.10.018>.
- [45] A. Antosova, M. Gancar, Z. Bednarikova, J. Marek, D. Zahn, S. Dutz, Z. Gazova, Surface-modified magnetite nanoparticles affect lysozyme amyloid fibrillation, *Biochim. Et. Biophys. Acta (BBA) - Gen. Subj.* 1865 (2021) 129941, <https://doi.org/10.1016/j.bbagen.2021.129941>.
- [46] A. Antosova, Z. Bednarikova, M. Koneracka, I. Antal, V. Zavisova, M. Kubovcikova, J.W. Wu, S.S.-S. Wang, Z. Gazova, Destroying activity of glycine coated magnetic nanoparticles on lysozyme, α -lactalbumin, insulin and α -crystallin amyloid fibrils, *J. Magn. Magn. Mater.* 471 (2019) 169–176, <https://doi.org/10.1016/j.jmmm.2018.09.096>.
- [47] G. Gao, M. Zhang, D. Gong, R. Chen, X. Hu, T. Sun, The size-effect of gold nanoparticles and nanoclusters in the inhibition of amyloid- β fibrillation, *Nanoscale* 9 (2017) 4107–4113, <https://doi.org/10.1039/C7NR00699C>.
- [48] Y. Kim, J.H. Park, H. Lee, J.M. Nam, How do the size, charge and shape of nanoparticles affect amyloid β aggregation on brain lipid bilayer?, 2016 6:1, *Sci. Rep.* 6 (2016) 1–14, <https://doi.org/10.1038/srep19548>.
- [49] H.R. Kalhor, A. Yahyazadeh, Investigating the effects of amino acid-based surface modification of carbon nanoparticles on the kinetics of insulin amyloid formation, *Colloids Surf. B Biointerfaces* 176 (2019) 471–479, <https://doi.org/10.1016/j.colsurfb.2019.01.033>.
- [50] S.S. Lu, Y.-R. Lai, L.-H. Hsiao, H.-Y. Huang, Y.-H. Tsai, Y. Chen, S.S.-S. Wang, Y.-C. Yeh, S.-L. Tsai, Effects of amino acid-functionalized silver nanoparticles on lysozyme amyloid fibrillogenesis, *Colloids Surf. B Biointerfaces* 222 (2023) 113144, <https://doi.org/10.1016/j.colsurfb.2023.113144>.
- [51] W.-H. Xi, G.-H. Wei, Amyloid- β peptide aggregation and the influence of carbon nanoparticles, *Chin. Phys. B* 25 (2016) 018704, <https://doi.org/10.1088/1674-1056/25/1/018704>.
- [52] T. John, J. Adler, C. Elsner, J. Petzold, M. Krueger, L.L. Martin, D. Huster, H. J. Risselada, B. Abel, Mechanistic insights into the size-dependent effects of nanoparticles on inhibiting and accelerating amyloid fibril formation, *J. Colloid Interface Sci.* 622 (2022) 804–818, <https://doi.org/10.1016/j.jcis.2022.04.134>.
- [53] R. Vácha, S. Linse, M. Lund, Surface effects on aggregation kinetics of amyloidogenic peptides, *J. Am. Chem. Soc.* 136 (2014) 11776–11782, <https://doi.org/10.1021/ja505502e>.
- [54] S. Radic, T.P. Davis, P.C. Ke, F. Ding, Contrasting effects of nanoparticle–protein attraction on amyloid aggregation, *RSC Adv.* 5 (2015) 105489–105498, <https://doi.org/10.1039/C5RA20182A>.
- [55] H.R. Barros, M. Kokkinopoulou, I.C. Riegel-Vidotti, K. Landfester, H. Thérien-Aubin, Gold nanocolloid–protein interactions and their impact on β -sheet amyloid

- fibril formation, RSC Adv. 8 (2018) 980–986, <https://doi.org/10.1039/C7RA11219J>.
- [56] V. Vetri, C. Canale, A. Relini, F. Librizzi, V. Militello, A. Gliozzi, M. Leone, Amyloid fibrils formation and amorphous aggregation in concanavalin A, Biophys. Chem. 125 (2007) 184–190, <https://doi.org/10.1016/j.bpc.2006.07.012>.
- [57] R. Khurana, C. Ionescu-Zanetti, M. Pope, J. Li, L. Nielson, M. Ramírez-Alvarado, L. Regan, A.L. Fink, S.A. Carter, A general model for amyloid fibril assembly based on morphological studies using atomic force microscopy, Biophys. J. 85 (2003) 1135–1144, [https://doi.org/10.1016/S0006-3495\(03\)74550-0](https://doi.org/10.1016/S0006-3495(03)74550-0).
- [58] J. Majorosova, V.I. Petrenko, K. Siposova, M. Timko, N. Tomasovicova, V. M. Garamus, M. Koralewski, M.V. Avdeev, B. Leszczynski, S. Jurga, Z. Gazova, S. Hayryan, C.-K. Hu, P. Kopcansky, On the adsorption of magnetite nanoparticles on lysozyme amyloid fibrils, Colloids Surf. B Biointerfaces 146 (2016) 794–800, <https://doi.org/10.1016/j.colsurfb.2016.07.024>.
- [59] M.-M. Mocanu, C. Ganea, K. Siposova, A. Filippi, E. Demjen, J. Marek, Z. Bednarikova, A. Antosova, I. Baran, Z. Gazova, Polymorphism of hen egg white lysozyme amyloid fibrils influences the cytotoxicity in LLC-PK1 epithelial kidney cells, Int J. Biol. Macromol. 65 (2014) 176–187, <https://doi.org/10.1016/j.ijbiomac.2014.01.030>.
- [60] M.F.M. Engel, C.P.M. van Mierlo, A.J.W.G. Visser, Kinetic and structural characterization of adsorption-induced unfolding of bovine α -lactalbumin, J. Biol. Chem. 277 (2002) 10922–10930, <https://doi.org/10.1074/jbc.M106005200>.
- [61] J. Woods, M. Mellon, Thiocyanate method for iron: a spectrophotometric study, Ind. Eng. Chem. Anal. Ed. 13 (1941) 551–554, <https://doi.org/10.1021/i560096a013>.
- [62] D. Nečas, P. Klapetek, Gwyddion: an open-source software for SPM data analysis, Open Phys. 10 (2012) 181–188, <https://doi.org/10.2478/s11534-011-0096-2>.
- [63] Gwyddion user guide, (n.d.). (<http://gwyddion.net/documentation/user-guide-en/index.html>) (Accessed 8 October 2024).
- [64] OriginLab - Origin and OriginPro - Data Analysis and Graphing Software, (n.d.). (<https://www.originlab.com/>) (Accessed 8 October 2024).